Check for updates

JGR Solid Earth

RESEARCH ARTICLE
10.1029/2024JB030767

Theoretical Modeling of Secondary Microseisms Considering Source and Receiver Site Structures, With a Focus on Ocean-Bottom Sediment Effects

Zongbo Xu[1], **Éléonore Stutzmann**[1], **Véronique Farra**[1], **and Wayne C. Crawford**[1]

[1]Université Paris Cité, Institut de physique du globe de Paris, CNRS, Paris, France

Key Points:

- Theoretical quantification of ocean-bottom sediments modulating secondary microseism Rayleigh waves at source and receiver sites differently
- The receiver site can amplify the energy by a factor of 100, also shown in field observations
- Accounting for these modulation effects improves the modeling of secondary microseisms

Supporting Information:

Supporting Information may be found in the online version of this article.

Correspondence to:

Z. Xu,
zongboxu@ipgp.fr

Citation:

Xu, Z., Stutzmann, É., Farra, V., & Crawford, W. C. (2025). Theoretical modeling of secondary microseisms considering source and receiver site structures, with a focus on ocean-bottom sediment effects. *Journal of Geophysical Research: Solid Earth*, *130*, e2024JB030767. https://doi.org/10.1029/2024JB030767

Received 15 NOV 2024
Accepted 10 APR 2025

Author Contributions:

Conceptualization: Zongbo Xu, Éléonore Stutzmann
Funding acquisition: Éléonore Stutzmann, Wayne C. Crawford
Investigation: Zongbo Xu
Methodology: Zongbo Xu, Éléonore Stutzmann, Véronique Farra
Project administration: Éléonore Stutzmann, Wayne C. Crawford
Software: Zongbo Xu, Éléonore Stutzmann
Writing – original draft: Zongbo Xu
Writing – review & editing: Zongbo Xu, Éléonore Stutzmann, Véronique Farra, Wayne C. Crawford

© 2025 The Author(s).
This is an open access article under the terms of the Creative Commons Attribution-NonCommercial License, which permits use, distribution and reproduction in any medium, provided the original work is properly cited and is not used for commercial purposes.

Abstract Opposite-direction oceanic wave interactions at the ocean surface generate microseisms between 0.1 and ~0.5 Hz, known as secondary microseisms (SM). SM recordings aid in imaging Earth's crust, but they also impede monitoring seismic signals due to tectonic activities. Thus, quantification of SM energy would benefit research in both areas. Previous studies on modeling SM energy have primarily focused on ocean modulation of SM, neglecting lateral variations in ocean and crustal structures between SM sources and seismic stations. In this study, we theoretically define source and receiver site coefficients which only depend on the local velocity model. Using these coefficients, we demonstrate how ocean-bottom sediments modulate the excitation and amplification of SM Rayleigh waves. A notable finding is that ocean-bottom sediments can amplify SM energy by a factor of 100, also supported by our field observation. We incorporate these modulation effects into modeling SM power spectral densities. Thanks to these theoretical improvements, our modeling matches field observations from both ocean-bottom seismometers and permanent land stations. This study potentially aids research on ambient seismic noise, ocean waves, and ocean-bottom seismic monitoring.

Plain Language Summary Ocean waves shake the Earth constantly, generating global low-frequency seismic waves. Between 0.1 and 1 Hz, these waves are excited by interactions between ocean waves traveling in opposite directions and are called “secondary microseisms” (SM). SMs can be used to image the Earth's crust, but can also mask signals from tectonic events beneath the oceans. Previous studies of SM amplitudes ignored the effects of sea floor sediments and assumed that the ocean thickness and crustal structure were the same at the SM sources and the measuring seismic stations. To improve our ability to understand and model SMs, we calculate how sediments and ocean thickness modulate the excitation of SM Rayleigh waves at the sources and their amplification at the stations. Our study indicates that ocean-bottom sediments can amplify SM energy by a factor up to 100. Incorporating these modulation effects into SM modeling, our synthetic SM energy matches well field observations from both ocean-bottom seismometers and permanent land stations. Our study provides insights into understanding SM energy and should help studies using ambient seismic noise imaging, ocean-bottom seismic monitoring, and ocean-wave modeling.

1. Introduction

In the absence of large earthquakes, global low-frequency (<1 Hz) seismic waves are predominantly driven by Earth's oceans. Ocean waves interacting either with the shallow seafloor or with each other generate seismic waves in two frequency bands: below 0.1 Hz and from 0.1 to approximately 0.5 Hz, respectively. Seismic waves in the first frequency band are further separated into Earth's hum (below ~0.05 Hz) and primary microseisms (from 0.05 to 0.1 Hz) (Ardhuin et al., 2015). In this study, we focus on seismic waves in the frequency band from 0.1 to ~0.5 Hz, normally known as secondary microseisms (SMs).

Rayleigh waves dominate seismic recordings of SMs. Processing these recordings using seismic interferometry at land stations (e.g., Bensen et al., 2007; Lin et al., 2008; Shapiro et al., 2005; Shen et al., 2016) or ocean bottom stations (e.g., Hable et al., 2019) provides Rayleigh-wave velocities and, sequentially, images of crustal velocity structures. Furthermore, since the seismic quality factor (Q) is important for understanding crustal thermal states, there have also been efforts to estimate Q values from SM recordings (e.g., Boschi et al., 2019; Prieto et al., 2009). However, there is an ongoing debate on whether these Q estimates accurately reflect crustal Q structures (e.g., Tsai, 2011; Viens et al., 2017). One way to address this issue is to better understand the input data for Q estimation: the SM amplitudes. Finally, high SM amplitudes impede detection of seismic events, especially when using ocean-bottom seismometers to monitor seismic signals from tectonic activities (e.g., Ide et al., 2007;

21699356, 2025, 5, Downloaded from https://agupubs.onlinelibrary.wiley.com/doi/10.1029/2024JB030767 by Portail BibCNRS INSU, Wiley Online Library on [11/06/2025]. See the Terms and Conditions (https://onlinelibrary.wiley.com/terms-and-conditions) on Wiley Online Library for rules of use; OA articles are governed by the applicable Creative Commons License

Kaneko et al., 2018; Webb, 1998; Webb & Crawford, 2010; Yarce et al., 2019). Theoretical quantification of SM amplitudes could assist such monitoring studies. It is worth noting that, while we focus on SM Rayleigh waves in this study, body waves also exist in SM recordings and have been extensively studied (e.g., Farra et al., 2016; Gerstoft et al., 2008; Gualtieri et al., 2014; Meschede et al., 2017; Nishida & Takagi, 2016).

The SM mechanism was first proposed by Longuet-Higgins (1950), that is, opposite-direction ocean gravity wave interactions generating pressure sources close to the ocean surface and these sources exciting seismic waves propagating through oceanic/continental crusts to a seismometer. This theory was later validated using SM recordings from permanent land stations (e.g., Ardhuin et al., 2011; Kedar et al., 2008; Stutzmann et al., 2012). Modeling SM in these studies, referred to as LH-SM modeling, employs a laterally homogeneous ocean-crust model for each source: an ocean layer overlying a solid halfspace. LH-SM modeling does not account for ocean-bottom sediments (Ardhuin et al., 2013; Gimbert & Tsai, 2015) or ocean-crust lateral heterogeneity, influencing SM amplitudes.

To address these issues, we theoretically demonstrate that ocean-bottom sediments significantly modulate Rayleigh-wave excitation and reception at the SM source and receiver sites, respectively (Section 2). Our theory improves LH-SM modeling, and we detail our implementation in Section 3. A comparison of our modeling results to field SM observations reveals that, compared to LH-SM modeling, our modeling better explains SM observations at both ocean-bottom seismometers and permanent land stations (Section 4). We also discuss how our study benefits other topics, such as Q estimation and the inversion of SM source distribution, and we propose improvements to our modeling (Section 5). Our study would benefit future seismic investigation of Q and seismic monitoring on the ocean bottom.

2. Methodology

The power spectral density (PSD) of secondary microseisms (SMs) recorded at a station ($\mathbf{x_r}$) is written as:

$$F(\mathbf{x_r},f) = \int_0^{2\pi}\int_0^{\pi} F_P(\mathbf{x_s},f)\sum_i |G^i_{ZZ}(\mathbf{x_r},\mathbf{x_s},f)|^2 R_E^2 \sin\psi d\lambda d\psi, \quad (1)$$

where F_P is the SM pressure source PSD at seismic-wave frequency f and is in units of $Pa^2m^2Hz^{-1}$, for ocean-surface SM sources at $\mathbf{x_s}$ (Hasselmann, 1963; Longuet-Higgins, 1950). For SM Rayleigh waves, $G^i_{ZZ}(\mathbf{x_r},\mathbf{x_s})$ is the ith-mode Rayleigh-wave Green's function representing the vertical-component displacement response at $\mathbf{x_r}$ due to a pressure source at $\mathbf{x_s}$. We consider fundamental and 1st-higher mode Rayleigh waves in this study. R_E is Earth's radius, and ψ and λ represent the colatitude and longitude of a potential SM source location; $R_E^2 \sin\psi d\lambda d\psi$ is the surface area of this potential source. It is worth noting that this integral is for the entire Earth's ocean surface, where F_p is nonzero.

2.1. Two Integrants: Pressure Source and Green's Function

The physics of the SM equation (Equation 1) includes two integrants: the SM pressure source PSD (F_P) and the Rayleigh-wave Green's function (G_{ZZ}). F_P is written as (Ardhuin et al., 2011; Farra et al., 2016; Hasselmann, 1963):

$$F_P(\mathbf{x_s},f) = (2\pi)^2\rho_w^2 g^2 f E^2(\mathbf{x_s},f/2)\int_0^{\pi} M(\mathbf{x_s},\phi,f/2)\,M(\mathbf{x_s},\phi+\pi,f/2)\,d\phi, \quad (2)$$

where ρ_w is ocean water density, g is Earth's gravity acceleration, $f/2$ is the frequency of ocean gravity waves, $E^2(\mathbf{x_s},f/2)$ is the sea-surface-elevation PSD at $\mathbf{x_s}$, and $M(\mathbf{x_s},\phi,f/2)$ is a non-dimensional ocean gravity-wave energy distribution at azimuth ϕ and frequency $f/2$. E and the integral in Equation 2 can be output from ocean-wave hindcasts (e.g., Ardhuin et al., 2011). Details of this equation can be found in Ardhuin et al. (2019). Note that the SM pressure sources are close to the ocean surface and thus the depth of $\mathbf{x_s}$ (z_s) is the same as sea level.

We adopt the Rayleigh-wave Green's function of a multi-layered and weakly laterally heterogeneous medium (e.g., Keilis-Borok, 1989; Woodhouse, 1974). The amplitude part of this function is written as:

$$|G^i_{ZZ}(\mathbf{x_r},\mathbf{x_s},f)| = \underbrace{\left[\frac{r_2(z_s)}{\sqrt{4\pi f c U I_1}}\right]^i_s}_{\text{Source site coefficient}} \underbrace{\frac{\pi f \exp[-\pi f t^*]}{\sqrt{2\pi k^i(\mathbf{x_r}) R_E \sin(\Delta)}}}_{\text{Geometric ray path}} \underbrace{\left[\frac{r_2(z_r)}{\sqrt{4\pi f c U I_1}}\right]^i_r}_{\text{Receiver site coefficient}} \quad (3)$$

where the superscript i of G_{ZZ} indicates that this whole equation is for the fundamental or 1st-higher mode Rayleigh wave. r_2 denotes the Rayleigh-wave vertical-component-displacement eigenfunction, representing the amplitude of this component varying with depth (e.g. Aki & Richards, 2002, Chapter 7), and I_1 denotes the wave energy (details of the eigenfunction and I_1 are in Appendix A). z_s and z_r are the source and receiver depths, respectively. The subscript s (r) means that the whole term inside the bracket is for the source (receiver) site. We refer to $C^i_s = \left[\frac{r_2(z_s)}{\sqrt{4\pi f c U I_1}}\right]^i_s$ and $C^i_r = \left[\frac{r_2(z_r)}{\sqrt{4\pi f c U I_1}}\right]^i_r$ in Equation 3 as source and receiver site coefficients of ith-mode Rayleigh waves, respectively. Note that our definition of these coefficients leads to their values independent of frequency for a homogeneous halfspace.

We assume that Rayleigh waves propagate along great-circle paths without mode conversion in such a weakly laterally heterogeneous medium. Δ is the arc distance in degrees between a SM source and a receiver, $k^i = 2\pi f / c^i(\mathbf{x_r})$ is the ith-mode wavenumber of the receiver site (Tromp & Dahlen, 1992), $\frac{1}{\sqrt{2\pi k^i R_E \sin(\Delta)}}$ accounts for geometric spreading in a spherically symmetric Earth (e.g., Snieder & Nolet, 1987; Zhou et al., 2004). c^i, U^i and Q^i are the ith-mode Rayleigh-wave phase and group velocities and quality factor, respectively. $t^* = \int \frac{R_E d\Delta}{U^i Q^i}$, and $\exp[-\pi f t^*]$ gives the ith mode Rayleigh-wave attenuation during its propagation. We only adopt the Green's function amplitude, because its phase is not used in modeling SM PSDs (Equation 1). Equation 3 is based on the far-field assumption. Thus, to satisfy this assumption, we remove the sources within 0.5° (55 km) distance from a receiver.

We refer to Equation 3 as WLHM Green's function in the following, because it corresponds to weakly laterally heterogeneous media. WLHM Green's function has been benchmarked against a wave-equation solver in an industry-scale study (El Khoury, 2022). To compute source and receiver site coefficients in Equation 3, we employ eigenfunction theory (e.g., Aki & Richards, 2002, Chapter 7) and three boundary conditions: zero pressure at the ocean surface, zero shear stress and continuous vertical stress and vertical displacement at the ocean bottom, and a radiation boundary condition at infinite depth (Biot, 1952). Details of this computation are in Appendix A. WLHM Green's function yields consistent results (Figures S6d and S7g in Supporting Information S1) with the analytical expression of the Rayleigh-wave Green's function for simplified 2-layer models (ocean and half space crust) employed by previous studies (e.g., Ardhuin et al., 2011; Longuet-Higgins, 1950; Stutzmann et al., 2012) (Appendix B). We detail how WLHM Green's function contributes to SM modeling in the following section.

2.2. Advantages of WLHM Green's Function

To illustrate WLHM Green's function (Equation 3), we adopt a simple three-layer model: an ocean layer overlying a sediment layer, over a bedrock half-space (Figure 1). We compute the source and receiver site coefficients of this model to quantify how the thicknesses of the ocean and sediment layers affect the Rayleigh-wave amplitude. In our computation, we fix the acoustic/body wave velocities and the density of each layer, but we vary thicknesses of the ocean and sediment layers, based on global model of ocean and ocean-bottom-sediment thicknesses. Hereafter we discuss the source and then the receiver site coefficients.

A higher source site coefficient represents a more efficient excitation of Rayleigh waves. A larger ocean thickness leads to the excitation peaking at a lower frequency (Figure S4 in Supporting Information S1), and the coefficients can vary by up to a factor of ~3 (e.g., at 0.1 Hz in Figure 1b), agreeing with the ocean resonance effect discussed in previous studies (Longuet-Higgins, 1950; Stutzmann et al., 2012). Sediments can amplify this excitation difference by up to a factor of 10 (e.g., at 0.25 Hz for 1,000-m-thick sediments in Figure 1b). Sediments beneath a thin ocean layer also modify the peak/resonance frequency of the source site coefficient (black curves in Figure 1b). For a thick ocean layer (4,000 m), a thicker ocean-bottom sediment layer results in a lower resonant frequency (around or even below 0.1 Hz). For the same ocean thickness, the source site coefficient is relatively

21699356, 2025, 5, Downloaded from https://agupubs.onlinelibrary.wiley.com/doi/10.1029/2024JB030767 by Portail BibCNRS INSU, Wiley Online Library on [11/06/2025]. See the Terms and Conditions (https://onlinelibrary.wiley.com/terms-and-conditions) on Wiley Online Library for rules of use; OA articles are governed by the applicable Creative Commons License

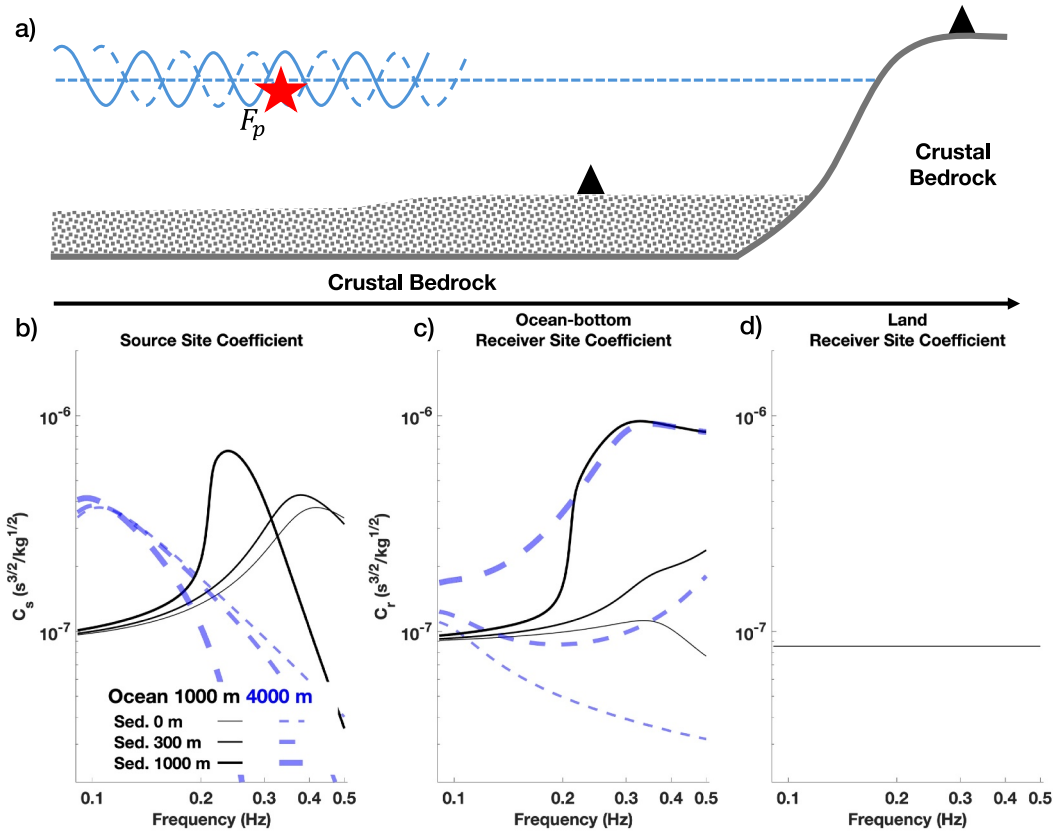

Figure 1. Illustration of secondary microseism (SM) source, ocean-bottom seismometer, and permanent land station (a). There are three layers on the ocean side: an ocean layer overlying a sediment layer on a crustal halfspace. To demonstrate the modulation effect of these ocean-sediment layers, we choose two ocean thickness values and three sediment-layer thickness values based on their global distributions (Figure S1 in Supporting Information S1). For each three-layer model, we compute the Rayleigh-wave group and phase velocities and the eigenfunctions (Figure A1, Figures S2 and S3 in Supporting Information S1). We calculate the fundamental-mode Rayleigh-wave source site coefficient at the ocean surface (b) and the receiver site coefficients at the ocean bottom (c). The coefficients for 1st-higher mode Rayleigh waves are in Figure S5 in Supporting Information S1. On the land side, only the halfspace exists and we also compute the receiver site coefficients on land surface (d). Products of these source and receiver site coefficients are in Figures S6 and S7 in Supporting Information S1, accounting for both the fundamental and 1st-higher mode Rayleigh waves. Acoustic/elastic parameters of these layers are listed in Table S1 in Supporting Information S1.

small at higher frequencies (e.g., >0.25-Hz blue dashed curves in Figure 1b), because of the low eigenfunction values at the ocean surface (Figures A1h and A1i). Note that at these frequencies, we need to consider 1st-higher-mode Rayleigh waves contributing to the SM energy (Figures S5–S7 in Supporting Information S1).

Receiver site coefficient indicates ground motion amplitudes caused by Rayleigh waves. A high correlation exists between the dominate frequencies of the coefficients and the ocean thickness (Figure S4 in Supporting Information S1). Additionally, we also observe a further amplification effect caused by an ocean-bottom sediment layer. Such a layer can amplify the ground motion at the ocean bottom by an order of magnitude (i.e., a factor of 10) (e.g., between 0.3 and 0.5 Hz in Figure 1c). We observe such amplification in field observations (Sections 4 and 5.2). Note that it has been reported that OBS recordings of earthquakes present large amplitudes (e.g., Nakamura et al., 2014; Takemura et al., 2023) and that Rayleigh-wave ground motions are amplified in continental sedimentary basins (Bowden & Tsai, 2017). Given that these studies focus on earthquake ground motions rather than microseisms, we recommend that readers refer to relevant studies on how these amplification phenomena may bias estimation of earthquake source properties (e.g., Abercrombie, 1997; Kubo et al., 2018; Nakamura et al., 2014) and may contribute to potential seismic hazards (e.g., Viegas et al., 2010).

21699356, 2025, 5, Downloaded from https://agupubs.onlinelibrary.wiley.com/doi/10.1029/2024JB030767 by Portail BibCNRS INSU, Wiley Online Library on [11/06/2025]. See the Terms and Conditions (https://onlinelibrary.wiley.com/terms-and-conditions) on Wiley Online Library for rules of use; OA articles are governed by the applicable Creative Commons License

21699356, 2025, 5, Downloaded from https://agupubs.onlinelibrary.wiley.com/doi/10.1029/2024JB030767 by Portail BibCNRS INSU, Wiley Online Library on [11/06/2025]. See the Terms and Conditions (https://onlinelibrary.wiley.com/terms-and-conditions) on Wiley Online Library for rules of use; OA articles are governed by the applicable Creative Commons License

2.3. Comparison With the Previous Studies

Previous studies on global-scale SM modeling have employed an analytical expression of the Rayleigh-wave Green's function for a laterally homogeneous two-layer model (e.g., Ardhuin et al., 2011; Kedar et al., 2008; Stutzmann et al., 2012). For each SM source, the Green's function corresponds to an ocean layer overlying a crustal halfspace and represents the ground motion at the ocean bottom (Longuet-Higgins, 1950). This Green's function cannot account for the impacts of the ocean-bottom sediments on the source and receiver site coefficients. Therefore, to match SM observations amplified by sediments, this Green's function would lead to an underestimation of seismic attenuation and/or an overestimation of ocean wave energy (Section 4).

Computation of Rayleigh-wave Green's function in the regional-scale SM modeling has been conducted using wave-equation solvers (e.g., Le Pape et al., 2021; Ying et al., 2014). Such solvers can incorporate lateral variations of ocean thicknesses and ocean-bottom sediments and thus accurately model how these structures affect SM amplitudes (Gualtieri et al., 2015). However, applying a wave-equation solver to all potential SM sources (i.e., the global ocean surface) is almost computationally prohibitive. Indeed, global-scale numerical simulations typically lack ocean layers (e.g., Ermert et al., 2017; Igel et al., 2021). Employing Equation 3 to model SM PSDs is more computationally feasible.

3. Implementation of SM PSD Modeling

Combining the SM pressure source PSD and WLHM Green's function improves the SM modeling. We present the implementation of this new modeling below, and we refer to this new modeling as WLHM modeling.

3.1. Computation of Pressure Source and Green's Function

SM pressure source PSDs (F_P in Equation 1) are an output from the WAVEWATCH III pre-computed ocean gravity wave hindcast (Wavewatch III Development Group, 2016). F_P distributions on Earth's ocean surface over 10 years are available at ftp://ftp.ifremer.fr/ifremer/ww3/HINDCAST/SISMO and are achieved with filenames ended with "p2l" in an expression (Ardhuin et al., 2011):

$$F_{p2l}(\mathbf{x_s},f) = \log_{10}\left[\rho_w^2 g^2 f E^2(\mathbf{x_s},f/2)\int_0^{\pi} M(\mathbf{x_s},\phi,f/2)\,M(\mathbf{x_s},\phi+\pi,f/2)\,d\phi\right]. \quad (4)$$

We calculate F_P as $(2\pi)^2 10^{F_{p2l}}$. Ocean gravity wave reflection at shorelines is a poorly constrained physical process that can significantly affect F_p (e.g., Ardhuin & Roland, 2012): we discuss how to address this uncertainty in Section 3.3.

WLHM modeling also requires the Rayleigh-wave Green's function including both source and receiver site coefficients (Equation 3). The source site coefficient is calculated at each potential source site based on a 1D model of an ocean layer over solid earth layers. We use the same bathymetry map adopted in the hindcast to obtain global ocean thicknesses (Figure 2a), with the water acoustic velocity and water density values from Longuet-Higgins (1950): 1,400 m/s and 1,000 kg/m^3, respectively. For the solid layers, such as sediments and bedrocks, we use the global crustal model CRUST1.0 (Laske et al., 2012). This crustal model divides Earth's surface into a 1-by-1-deg grid, with each grid cell consisting of sediment layers, crustal bedrock layers, and an upper-mantle halfspace. We present the source site coefficients of fundamental and 1st-higher mode Rayleigh waves for the global ocean in Figure 2 and Figure S9 in Supporting Information S1, respectively. We use these same models to calculate receiver site coefficients in the ocean areas. In the continental areas, we only use permanent land stations, normally deployed on bedrocks, and thus we remove sediment layers in CRUST1.0 if they exist. We discuss the maps of our source and receiver site coefficients in the following subsection. For computational simplicity, in calculating t^* (Equation 3), we use a constant value (1,800 m/s) for the fundamental and 1st-higher mode Rayleigh-wave group velocities. Note that calculating t^* also requires Q values, and we describe how to choose the values in Section 3.3.

3.2. Maps of Source and Receiver Site Coefficients

Our source site coefficient maps are clearly influenced by global ocean thickness. For example, ocean thickness along a mid-ocean ridge (MOR), (e.g., in Figure 2a), commonly varies between 3,000 and 4,000 m, smaller than

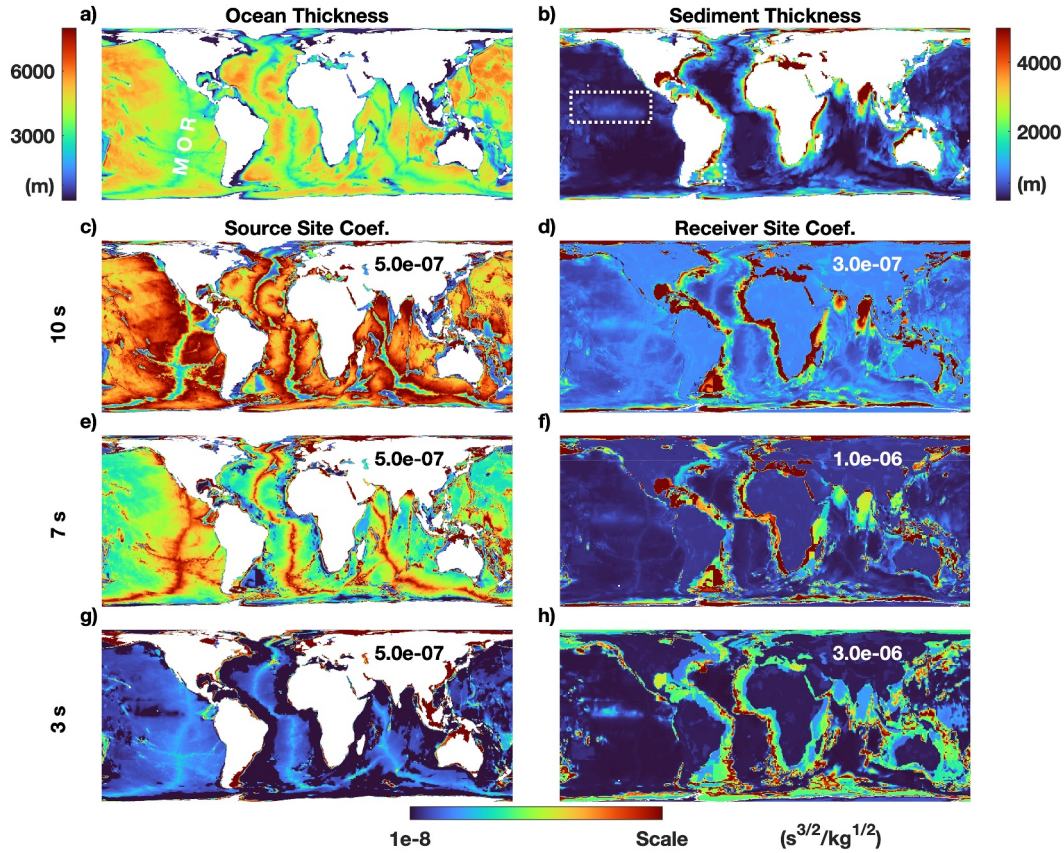

Figure 2. Maps of global ocean thickness (a), ocean-bottom sediment thickness (b), and fundamental mode Rayleigh-wave source and receiver site coefficients at three periods (c–h). We plot each coefficient map from 10^{-8} to a scale in the top-right corner of the subplot. The three source site coefficient maps share a same plotting range: from 10^{-8} to $5 * 10^{-7}$. The ocean thickness values are the ones used in WAVEWATCH III. The sediment thickness values are from CRUST1.0 (Laske et al., 2012), and the corresponding seismic velocities are in Figure S8 in Supporting Information S1. We present the source and receiver site coefficients of the 1st-higher-mode Rayleigh waves in Figure S9 in Supporting Information S1.

the nearby regions (~5,000 m). Since a thinner ocean layer leads to the source site coefficient peaking at a higher frequency (Figure 1b), low-frequency source site coefficients (0.1 Hz, i.e. 10 s period) are lower along a MOR than in neighboring regions (Figure 2c), whereas the higher frequency coefficients peak at the MORs (Figures 2e and 2g). We also observe the footprint of offshore sediments in our source site coefficients, for example, in the equatorial Pacific (white dashed rectangle in Figure 2b) and in offshore sedimentary basins near Brazil (white dashed square in Figure 2b), because thick sediments reduce the corresponding source site coefficient values at higher frequencies (e.g., Figure 1b).

Our receiver site coefficients are significantly amplified by offshore sediments, such as continental margin sediments, sediments in the Gulf of Mexico, the Equatorial Pacific and offshore sedimentary basins near Brazil (Figure 2h). This amplification is affected not only by the thickness of these sediments but also by their seismic-wave velocities (Figure S8 in Supporting Information S1). Ocean thickness also modulates the receiver site coefficients, especially at low frequencies like 0.1 Hz (Figure 1c). This is why the receiver site coefficient map at 0.1 Hz highlights the shape of the eastern Pacific MOR (Figure 2d).

Because we calculate our source and receiver site coefficient maps from CRUST1.0, artifacts in this model are inherently reflected in our maps. For example, an almost-latitudinal contrast exists in the sediment velocity maps from CRUST1.0 in the region of the Brazil offshore sedimentary basins, and therefore a similar shape exists in our coefficient maps (Figure S8 in Supporting Information S1). Crustal-model artifacts like this one may be removed in future higher-resolution crustal velocity models, and our maps could then be updated. Because CRUST1.0 is one of the most commonly used global crustal models, we continue employing it in this study.

21699356, 2025, 5, Downloaded from https://agupubs.onlinelibrary.wiley.com/doi/10.1029/2024JB030767 by Portail BibCNRS INSU, Wiley Online Library on [11/06/2025]. See the Terms and Conditions (https://onlinelibrary.wiley.com/terms-and-conditions) on Wiley Online Library for rules of use; OA articles are governed by the applicable Creative Commons License

21699356, 2025, 5, Downloaded from https://agupubs.onlinelibrary.wiley.com/doi/10.1029/2024JB030767 by Portail BibCNRS INSU, Wiley Online Library on [11/06/2025]. See the Terms and Conditions (https://onlinelibrary.wiley.com/terms-and-conditions) on Wiley Online Library for rules of use; OA articles are governed by the applicable Creative Commons License

3.3. Coefficients of Ocean-Wave Reflection and Seismic Attenuation

Two required physical parameters in modeling SM PSDs are the ocean gravity wave energy reflection coefficient at shorelines (denoted as R^2 and used in ocean-wave hindcasts) and the Rayleigh-wave quality factor (i.e., Q) used in Equation 3. Modeling SM PSDs would benefit from knowledge of the spatial distributions of these two parameters. However, these two parameters are poorly constrained, and accurate estimates of their spatial distributions are not yet available. To account for the contributions of Q and R^2 to the SM energy, we adopt spatially averaged values of Q and R^2 in the modeling, similar to the Q estimation in crustal attenuation studies (e.g., Erickson et al., 2004). However, because the SM sources are potentially distributed across the entire Earth's ocean surface, these two model parameters do not correspond to certain seismic paths or geological regions. We choose these two parameters from reasonable ranges so that they best explain the SM observations (see details in the next paragraph and field examples in Section 4). Even so, a trade-off exists between these two parameters (Stutzmann et al., 2012). A higher R^2 value results in greater ocean-wave reflection amplitudes, leading to stronger interactions between reflected and incident ocean gravity waves, thereby increasing SM source intensities and PSD values. A larger Q indicates less Rayleigh-wave energy attenuated along its propagation paths, thus increasing SM PSD values. Therefore, an increase/decrease in SM-PSD amplitude could be caused by a larger/smaller value of either R^2 or Q.

We search for an optimal combination of R^2 and Q, so that our synthetic results match the SM-PSD field observations, following previous SM PSD modeling (Stutzmann et al., 2012). We vary Q from 100 to 400, with a step size of 30. For each Q value, we loop through possible R^2 values. We conduct WLHM modeling using SM pressure source PSDs based on two sets of WAVEWATCH III hindcasts. In one hindcast setting, $R^2 = 0$, that is, no ocean gravity wave reflections occur at shorelines. In the other setting, R^2 is varied spatially according to three types of shoreline environments: 40% for the nearly vertical sides of icebergs, 20% for the shorelines of islands smaller than 0.5 deg in latitude and longitude, and 10% for the shorelines of continents and larger islands (Ardhuin et al., 2011). These two hindcast settings serve as end members for ocean-wave modeling scenarios due to R^2 variation (Ardhuin et al., 2011). We compute the SM synthetics for these 2 hindcast settings and a range of Q values, then use a linear interpolation between the end member synthetics to compute synthetics for varying R^2 coefficients (keeping the fixed proportionality for iceberg, small island, and continental shorelines). We then define our misfit function between our synthetic and field spectrograms as

$$\chi = \frac{1}{N}\sum_{t_1}^{t_N}\frac{|\sqrt{I^s}-\sqrt{I^o}|}{\sqrt{I^o}} \tag{5}$$

$$= \frac{1}{N}\sum_{t_1}^{t_N}\frac{\left|\sqrt{\int_{f_1}^{f_2}F^s(f)df}-\sqrt{\int_{f_1}^{f_2}F^o(f)df}\right|}{\sqrt{\int_{f_1}^{f_2}F^o(f)df}} \tag{6}$$

where I^s and I^o are integrals of the synthetic (s) and observed (o) SM displacement PSDs from frequency f_1 to f_2 (i.e., SM energy). In this study, we adopt $f_1 = 0.1$ Hz and $f_2 = 0.33$ Hz. We stop at 0.33 Hz, because Rayleigh waves at this frequency (or at a higher one) would behave like Scholte waves (Scholte, 1958) in extreme cases where both a thick ocean and a thick sediment layer are present (Figure A1i). The summation in Equation 6 is over all time windows used to compute SM PSDs. F^s is WLHM modeling of SM PSD (Equation 1). When computing observed PSDs (F^o), we use a time window length of 1 hr, and we use all available data of one station over 1 year. We exclude time windows presenting PSD amplitudes 10 thousand times larger than the median of PSDs across all time windows, to avoid transient events (such as earthquakes or glitches) from biasing our estimate of F^o. We choose displacement over acceleration in our misfit function, because an acceleration PSD equals ω^4 times the corresponding displacement PSD, and thus higher-frequency content would dominate both the acceleration PSD integrals and the misfit function. Note that we compute one-sided PSDs.

4. Modeling of SM PSD

We present in this section that our WLHM modeling better explains the field observations at both ocean-bottom seismometers (OBSs) and permanent land stations, compared to the LH-SM modeling in previous studies.

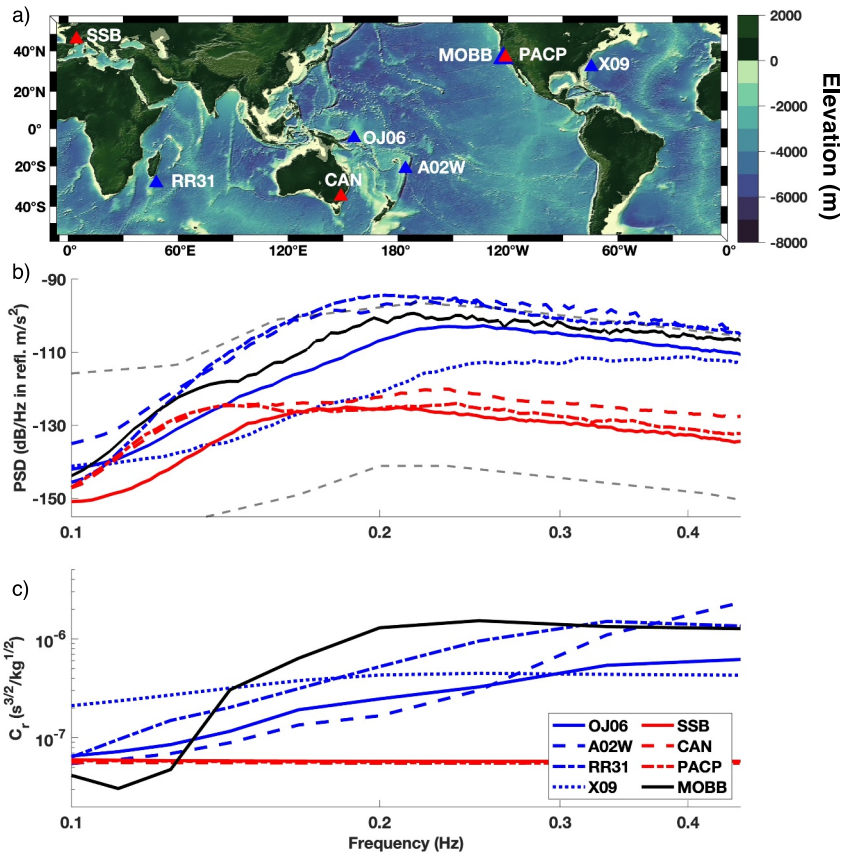

Figure 3. Location (a), one-sided power spectral densities (PSDs, b), and fundamental mode Rayleigh-wave receiver site coefficients (c) of seismic stations used in our study (Table 1). The coefficients for 1st-higher-mode Rayleigh waves are in Figure S10 in Supporting Information S1. MOBB and PACP are spatially close, so their symbols overlap on the map, though MOBB is an OBS and PACP is on the US continent (a). The dashed gray curves (b) are the high and low noise models from Peterson (1993). PSD of every station is the median of the corresponding observed acceleration spectrogram at each frequency (Figures 4 and 5, Figure S11 in Supporting Information S1).

Because OBS recordings are generally noisy, we select OBSs whose data quality has been validated as high by previous studies (Figure 3a, Table 1). Note that PSDs of the permanent land stations are indeed comparable to those of OBSs in magnitude between 0.1 and 0.15 Hz (between ~7 and 10 s period). However, the OBS PSD values are significantly higher than those of the land stations at frequencies over 0.15 Hz (Figure 3b). At 0.25 Hz, the PSDs of all the OBSs (except X09) are approximately 100 times (20 dB) greater than those of the land stations.

4.1. OBS Recordings

We use OBS stations located in various regions: the southern Indian Ocean (RR31), the western Pacific Ocean (OJ06, A02W), the northeastern Pacific Ocean (MOBB), and the northwestern Atlantic Ocean (X09). The ocean thickness at these stations ranges from ~800 to ~4500 m. The ocean-bottom sediments beneath these stations vary in thickness, from ~300 to ~4000 m. In this section, we focus on stations OJ06, A02W, and RR31 (Figure 4); we discuss stations X09 and MOBB in Section 5. Although a new velocity model is available beneath A02W (Zha & Webb, 2016), we still use model parameters from CRUST1.0, to maintain consistency.

In matching the field SM data of these stations, the WLHM modeling provides not only a good match to the seasonal variation of the PSD values (Figure 4), thanks to the SM pressure source modeling, but also good agreement with the SM displacement integrals (Figures 6a–6c). The misfits between our synthetic results and the corresponding field observations are smaller than 0.35 (Table 1). As a comparison, to reach this misfit level, the LH-SM modeling requires the upper bounds of R^2 and Q, while the synthetic spectra are still substantially lower

21699356, 2025, 5, Downloaded from https://agupubs.onlinelibrary.wiley.com/doi/10.1029/2024JB030767 by Portail BibCNRS INSU, Wiley Online Library on [11/06/2025]. See the Terms and Conditions (https://onlinelibrary.wiley.com/terms-and-conditions) on Wiley Online Library for rules of use; OA articles are governed by the applicable Creative Commons License

Table 1
Information of Seismic Stations in Our Study

Station	Network	Ocean thickness (m)	Sediment thickness (m)/V_S (m/s)	Spatially averaged Q (100–400)	Spatially averaged R^2 (0 − 10%)	Misfit	Quality check reports
OBS							
OJ06	PS	1,879	950/900	130 (400)	9.0% (10.0%)	0.24 (0.26)	Suetsugu et al. (2018)
A02W	YL	2,019	290/340	130 (400)	6.0% (10.0%)	0.26 (0.37)	Zha and Webb (2016)
RR31	YV	2,796	760/550	100 (400)	10.0% (10.0%)	0.27 (0.28)	Stähler et al. (2016)
X09	YO	4,587	3,750/1,110	100 (250)	6.5% (8.5%)	0.32 (0.25)	Lynner et al. (2020)
MOBB	BK	832	1,050/550	100 (400)	1.0% (10.0%)	0.48 (0.42)	Romanowicz et al. (2006)
Permanent Land stations							
SSB	G	0	0	160 (190)	0.5% (2.0%)	0.47 (0.32)	
CAN	G	0	0	130 (100)	2.0% (10.0%)	0.27 (0.25)	
PACP	BK	0	0	100 (100)	1.0% (3.0%)	0.43 (0.46)	

Note. The ocean thickness values are the ones used in WAVEWATCH III. The ocean-bottom sediment thicknesses of OBSs and the corresponding shear-wave velocity (V_S) are retrieved from CRUST1.0 (Laske et al., 2012). The spatially averaged values of Q and R^2 are obtained by minimizing the misfit (Equation 6) between WLHM modeling and the field observations (Figure 6 and Figure S12 in Supporting Information S1). We also present Q and R^2 from the LH-SM modeling in parenthesis next to the values from WLHM modeling. We present the modeling for all stations in Section 4 except for MOBB, which is in Section 5.2.

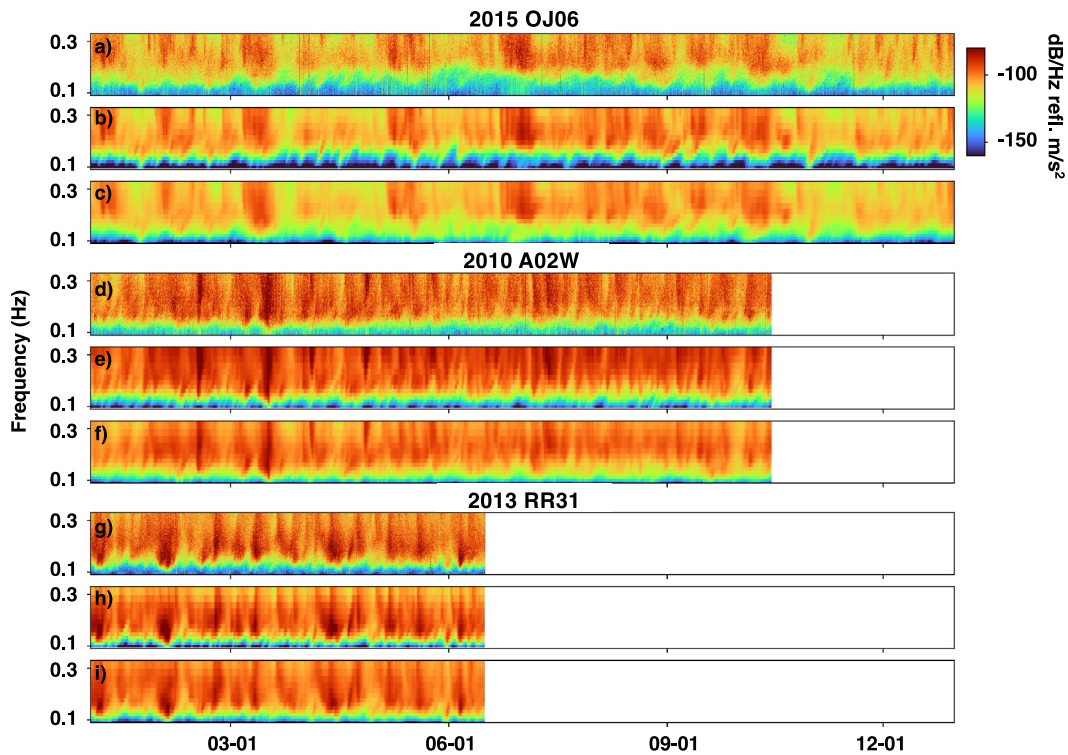

Figure 4. Observed and synthetic acceleration spectrograms of OBS stations OJ06, A02W, and RR31. For each station, the first row (a, d, g) corresponds to the observation, and the second (b, e, h) and third (c, f, i) rows are modeling results from the WLHM modeling and the LH-SM modeling, respectively. Note that each station's observations are from different years: 2015, 2010, and 2013.

21699356, 2025, 5, Downloaded from https://agupubs.onlinelibrary.wiley.com/doi/10.1029/2024JB030767 by Portail BibCNRS INSU, Wiley Online Library on [11/06/2025]. See the Terms and Conditions (https://onlinelibrary.wiley.com/terms-and-conditions) on Wiley Online Library for rules of use; OA articles are governed by the applicable Creative Commons License

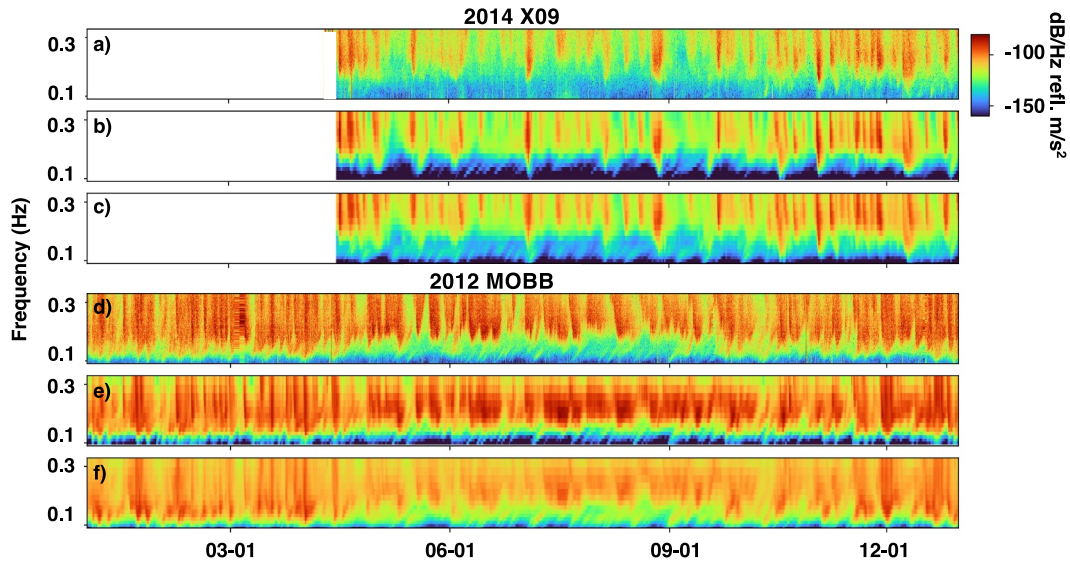

Figure 5. Observed and synthetic acceleration spectrograms of OBS stations X09 and MOBB. All plotting parameters match those in Figure 4.

in amplitude than the corresponding field observations above 0.2 Hz (Figures 4c, 4f, and 4i). These all support the superiority of WLHM modeling in explaining OBS recordings.

The LH-SM modeling requires the highest bounds of Q and R^2, to generate the highest possible SM Rayleigh-wave energy. This is partly due to the high receiver site coefficients at the OBS sites (Figure 3c). Without considering this amplification, achieving the same PSD values using LH-SM modeling requires larger values of Q and R^2, leading to overestimation of these parameters. Matching WLHM modeling to the field data provides estimates of Q and R^2 within reasonable ranges.

Our Q and R^2 estimates reflect spatially averaged values, rather than the R^2 of a specific shoreline or the Q of a certain Rayleigh-wave propagation path. We discuss how to further constrain Q in Section 5.3. Interpretations of these estimates are beyond the scope of our study, which is focused on improving our understanding of SM amplitudes.

4.2. Permanent Land Stations

We use land stations located in France (SSB), eastern Australia (CAN), and the west coast of the USA (PACP). The SM recordings from these stations are explained using the WLHM modeling as well as the LH-SM modeling (Figure 6, Figure S11 in Supporting Information S1). The estimates of Q from the WLHM modeling are also close to those from the LH-SM modeling (Table 1). However, the R^2 estimates from the LH-SM modeling are 3 or 4 times as large as ours. Even so, both models agree that the R^2 values for CAN and PACP are larger than that for SSB, indicating the ocean gravity wave reflection for CAN and PACP is stronger compared to that for SSB. This relationship between CAN and SSB has been shown in previous studies (e.g., Stutzmann et al., 2012). PACP is ~40 km from Monterey Bay in California, and R^2 along the Californian shoreline exhibits a wide variation, ranging between 1% and 36%, based on buoy data (Ardhuin & Roland, 2012). Thus, it is not surprising that the R^2 estimates from the WLHM and the LH-SM models are within this range. We discuss why the LH-SM modeling could match SM observation of permanent land stations in Section 5.4.

The Q estimates for PACP from both the WLHM and the LH-SM modeling are at the lower bound of the Q range. A similarly low Q value has been invoked before to explain field observations from another permanent station (BKS) in California, using the LH-SM modeling (Ardhuin et al., 2011). We emphasize that the Q estimates from either WLHM or LH-SM modeling represent a spatially averaged Q between all SM sources and a station. Furthermore, this Q estimate for land stations is also influenced by the energy loss during Rayleigh waves propagating from the oceanic crust to the continental crust, and neither WLHM modeling nor LH-SM

21699356, 2025, 5, Downloaded from https://agupubs.onlinelibrary.wiley.com/doi/10.1029/2024JB030767 by Portail BibCNRS INSU, Wiley Online Library on [11/06/2025]. See the Terms and Conditions (https://onlinelibrary.wiley.com/terms-and-conditions) on Wiley Online Library for rules of use; OA articles are governed by the applicable Creative Commons License

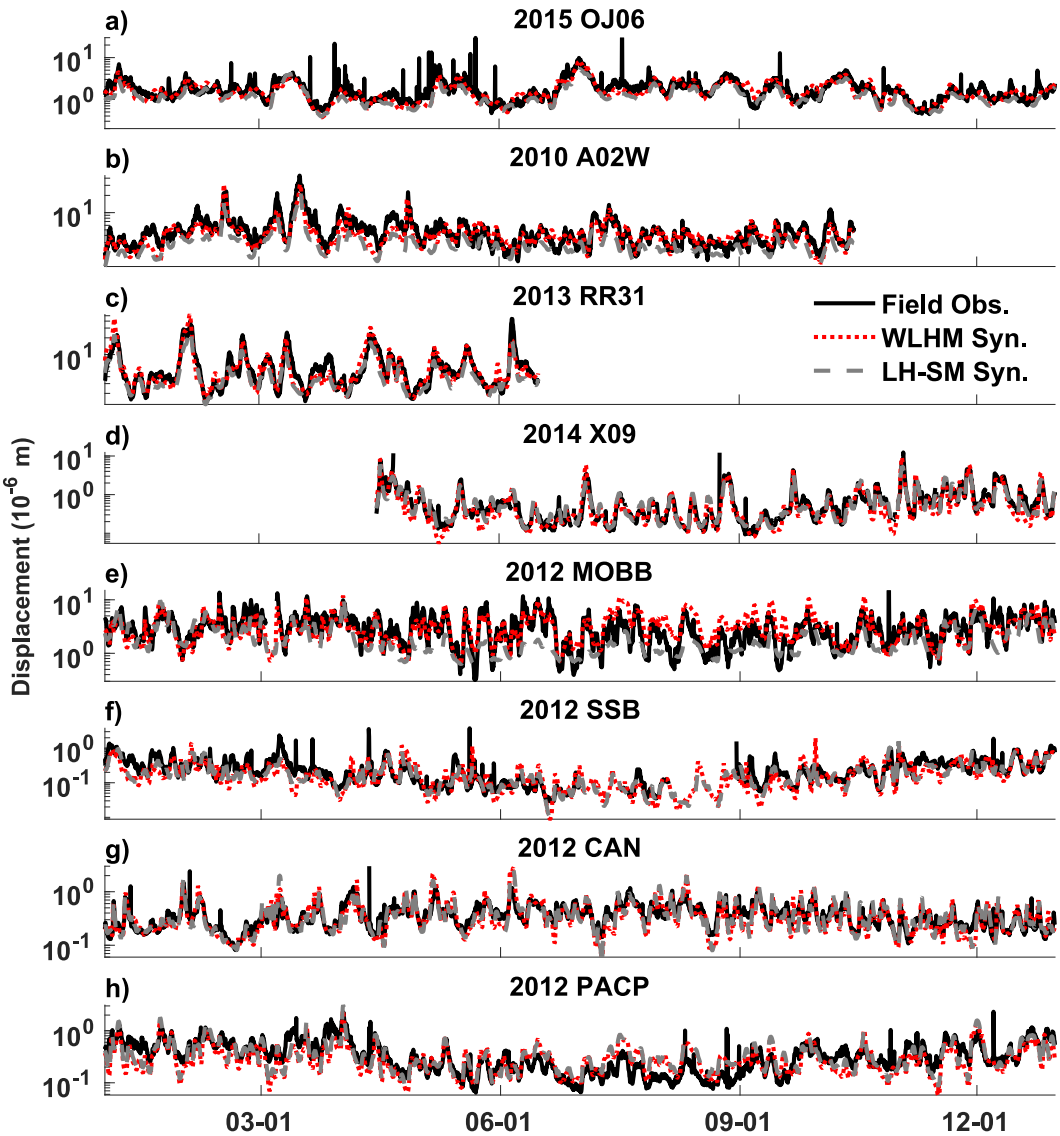

Figure 6. Comparison of the displacement integral between 0.1 and 0.33 Hz among the 8-station observation and the corresponding synthetics from our WLHM modeling and the LH-SM modeling. Misfits of these modelings are presented in Figure S12 in Supporting Information S1 and Table 1.

modeling considers this energy loss, leading to an underestimation of Q values. Therefore, a physical interpretation of these Q estimates requires further work, as we discuss in Section 5.3.

5. Discussion

The field examples above demonstrate that WLHM modeling can explain SM field observations in different environments (at the ocean bottom or on land) and across various regions. Hereafter we discuss two examples where WLHM modeling and LH-SM modeling give similar misfits (Section 5.1, 5.2, 5.3). We also present, based on our theory, why LH-SM modeling can match SM observations within a specific frequency band (Section 5.4) and how our study can benefit other research areas (Sections 5.5 and 5.6).

5.1. The Apparent Paradox of OBS Station X09

Among all of our OBS stations, station X09 overlies the thickest sediments (Table 1), yet has the lowest PSD value between 0.12 and 0.4 Hz (Figure 3b). The reason for this apparent paradox is two-fold. First, the receiver

21699356, 2025, 5, Downloaded from https://agupubs.onlinelibrary.wiley.com/doi/10.1029/2024JB030767 by Portail BibCNRS INSU, Wiley Online Library on [11/06/2025]. See the Terms and Conditions (https://onlinelibrary.wiley.com/terms-and-conditions) on Wiley Online Library for rules of use; OA articles are governed by the applicable Creative Commons License

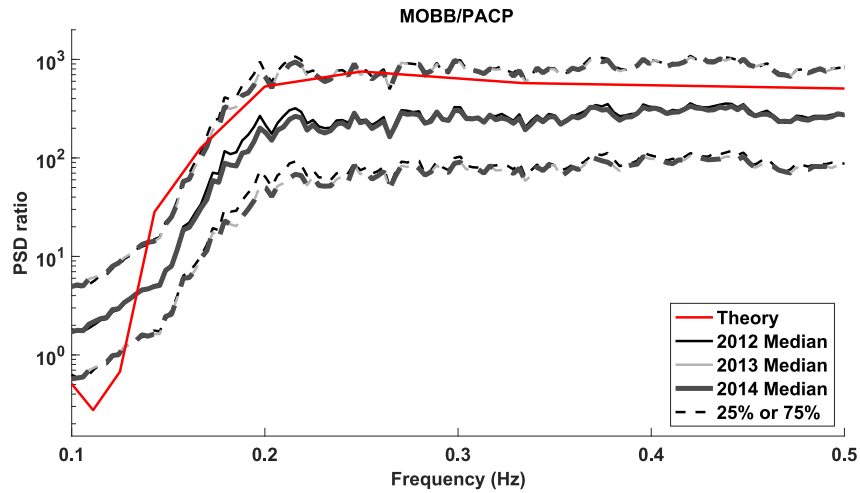

Figure 7. Theoretical (red) and observed (black, gray) receiver site amplification of MOBB relative to PACP. We plot 25th, 50th (i.e., median), and 75th percentiles across the PSD ratios from the field observations in 2012, 2013, and 2014.

site coefficient at X09 is comparable to, rather than lower than, at the other sites, because of relatively large sediment shear-wave velocity values (V_S) beneath X09 (>1,000 m/s). For comparison, the V_S values of the sediment layers beneath the other OBSs are 900 m/s (OJ06), 550 m/s (RR31), and 340 m/s (A02W).

Second, the shoreline reflectivity near X09 is comparable or lower than at the other three sites (OJ06, A02W, and RR31). It has already been noted that ocean gravity wave reflections are generally weak along the east coast of the US (Ardhuin & Roland, 2012). We attribute X09's low PSD values to its small SM pressure source PSDs contributed by the weak ocean gravity wave reflection. This hypothesis could be examined by future buoy measurements along this shoreline.

5.2. Large Site Amplification Energy Ratio at OBS Sites

Our theory reveals that the OBS site amplification energy ratio can be up to 100 with respect to permanent land stations, agreeing with the observations in Section 4 (Figure 3b). However, because our stations are located in various regions, the SM sources impacting each station may vary. To demonstrate this amplification more rigorously, we compare SM recordings at land station PACP with those of a nearby OBS station, MOBB, deployed in the California nearshore. The distance between these two stations is 86 km. Thus, the SM sources contributing to the observations at these two stations are likely similar or even identical. Rayleigh-wave attenuation in the SM frequency band over this distance is much smaller than the amplification energy ratio. For example, if we assume $Q = 100$ and a 1.8 km/s group velocity, 0.1 and 0.33 Hz Rayleigh-wave energy would lose 26% and 60%, respectively, when propagating from MOBB to PACP. Therefore, any SM PSD difference between these two station that is larger than a factor of 2–3 is mainly due to different receiver site coefficients. The MOBB station has been active for about 15 years, providing a rare long-duration OBS observation that allows us to evaluate the site amplification effect over multiple years.

We estimate the MOBB site amplification using the data from MOBB and PACP between 2012 and 2014. For the data in each year, we compute spectrograms of these two stations using one-hour-long time windows, calculate the PSD ratios of each time window, and then extract the values corresponding to three statistical percentiles: 25%, median, and 75% (Figure 7). These statistical values provide a frequency-dependent MOBB site amplification, relative to PACP, which is statistically the same in each of the 3 years.

We calculate the theoretical value as the square of the ratio of the theoretical fundamental-mode receiver site coefficients at the two sites: $\left(C_r^{MOBB}/C_r^{PACP}\right)^2$ (Figure 7). The theoretical ratio has a similar frequency-dependence as the measured ratio but it is more extreme, with values close to the 25th percentile of the measured ratio between 0.1 and 0.13 Hz, and close to the 75th percentile between 0.18 and 0.3 Hz. In the higher frequency band, our theory overestimates the site amplification. This overestimation could be due to an inaccurate

21699356, 2025, 5, Downloaded from https://agupubs.onlinelibrary.wiley.com/doi/10.1029/2024JB030767 by Portail BibCNRS INSU, Wiley Online Library on [11/06/2025]. See the Terms and Conditions (https://onlinelibrary.wiley.com/terms-and-conditions) on Wiley Online Library for rules of use; OA articles are governed by the applicable Creative Commons License

21699356, 2025, 5, Downloaded from https://agupubs.onlinelibrary.wiley.com/doi/10.1029/2024JB030767 by Portail BibCNRS INSU, Wiley Online Library on [11/06/2025]. See the Terms and Conditions (https://onlinelibrary.wiley.com/terms-and-conditions) on Wiley Online Library for rules of use; OA articles are governed by the applicable Creative Commons License

velocity model beneath MOBB. This overestimation also leads to our synthetic spectrum amplitudes being higher than the observed values.

Optical-fiber-based subsurface investigations have been conducted near MOBB (e.g., Cheng et al., 2021; Lindsey et al., 2019). An accurate characterization of the crustal structure using these data is promising (Romanowicz et al., 2023) and could provide more reliable receiver site coefficients at MOBB.

5.3. Future Improvements

One assumption in using WLHM Green's function is that no Rayleigh-wave reflection or mode conversion occurs when the waves propagate across shorelines. This assumption clearly simplifies this complex physics process, in which both reflection and mode conversion could occur (e.g., Gualtieri et al., 2015; Le Pape et al., 2021; Noguchi et al., 2016). These phenomena could cause the waves to be back-scattered into the ocean, therefore reducing SM energy recorded at land stations (Section 4.2). To quantify this back-scattered energy, a comprehensive study of Rayleigh waves propagating through shorelines would be needed, taking into consideration 3D wave propagation and shoreline geometry. Based on our knowledge, such a study is absent to date.

The Rayleigh-wave propagation in our modeling could also be more sophisticated. We assume that Rayleigh waves propagate along great-circle paths, which avoids ray tracing and simplifies the computation of the geometric ray path term in Equation 3. Sharp lateral heterogeneities will make Rayleigh waves propagate off of the great-circle paths or even propagate on multiple paths (Cotte et al., 2000; Pavlis & Mahdi, 1996; Woodhouse & Wong, 1986; Xia et al., 2018). Incorporating these propagation phenomena into WLHM modeling would require ray tracing for all potential SM sources (the global ocean surface), improving propagation modeling at the cost of computational speed. Ray tracing would also allow us to incorporate the spatial variation of the Rayleigh-wave group velocity (U), leading to a more accurate computation of t^* (Equation 3) and better constraining Rayleigh-wave attenuation in WLHM modeling.

The crustal velocity model used in WLHM modeling affects source and receiver site coefficients and therefore our synthetic result, as discussed in Sections 3.2 and 5.2. To improve the crustal model beneath an OBS station and better characterize the site amplification (Section 5.2), one could use inversions of compliance due to ocean gravity wave below 0.1 Hz (e.g., Crawford et al., 1991) and/or of admittance due to SM Rayleigh-wave propagation (e.g., Ruan et al., 2014). Note that velocity models obtained from these inversions should also align with petrophysical knowledge of sediments and rocks in oceanic environments.

WLHM modeling could be applied to studying short-period (<3 s) microseisms (e.g., Ardhuin et al., 2013; Gimbert & Tsai, 2015). To achieve this, besides of the aspects mentioned above in this subsection, we also need to consider conversion between Scholte waves and Rayleigh waves during their propagation, especially where thick ocean-bottom sediments are present like near-shore regions (e.g., Gualtieri et al., 2015). Meanwhile, local winds may lead to short-period ocean gravity waves. These waves are not the focus of global-scale ocean wave hindcast like WAVEWATCH III. Thus, incorporating these waves into SM modeling requires a regional ocean gravity hindcast, such as Booij et al. (1996) and/or reparameterization of WAVEWATCH III (Alday & Ardhuin, 2023; Romero, 2019).

5.4. Why Does LH-SM Modeling Work in a Narrow Frequency Band?

LH-SM modeling, based on a simple two-layer model of an ocean layer overlying a crustal halfspace, has been shown to match PSD observations at permanent land stations for frequencies between 0.1 and 0.2 Hz (5–10 s period). Based on our Green's function computations and the fact that the majority of global ocean thicknesses are around 4,000 m, the source site coefficients in this frequency band are approximately the same ($\sim 3 * 10^{-7}$ in Figure 1b) for ocean-bottom sediment thicknesses from 0 to 1,000 m. In addition, the reported LH-SM models only use seismic recordings from permanent land stations, normally deployed on crustal bedrock whose receiver site coefficients have the same order of magnitude (10^{-7}, Figure 3c) in this frequency band. These two aspects explain why the modeling can match the SM PSDs between 0.1 and 0.2 Hz.

5.5. Improving Q Estimation Based on Seismic Interferometry

The accuracy of applying seismic interferometry (SI) to SM recordings to estimate Q has been in debate. This estimation is based on the 1D-structure assumption and relies on SM amplitudes as an input. Notably, our study

21699356, 2025, 5, Downloaded from https://agupubs.onlinelibrary.wiley.com/doi/10.1029/2024JB030767 by Portail BibCNRS INSU, Wiley Online Library on [11/06/2025]. See the Terms and Conditions (https://onlinelibrary.wiley.com/terms-and-conditions) on Wiley Online Library for rules of use; OA articles are governed by the applicable Creative Commons License

clearly demonstrates how local sediments beneath a seismometer amplify SM amplitudes, especially for ocean-bottom seismometers. Thus, in future studies regarding this estimation, frequency-dependent site amplification needs to be considered both theoretically and in practice (e.g., Bowden et al., 2017).

5.6. Implications for the Calculation of SM Source Distributions

Our study directly incorporates SM pressure sources (Equation 1) derived from ocean wave hindcasts. Other studies invert field observations of SM to calculate the SM source distribution, using the Green's functions determined from numerical simulations (Ermert et al., 2016; Igel et al., 2021, 2023). In these simulations, the sources are typically positioned at the ocean bottom, rather than at the ocean surface as indicated by the SM mechanism, because it is computationally expensive to incorporate ocean layers. The inversion results are therefore hypothetical forces at the ocean bottom which generate SM recordings similar to those of the true SM pressure sources at the ocean surface (e.g., Igel et al., 2021). Furthermore, if these studies do not consider ocean-bottom sediments, their estimates might be biased in intensity and location.

Our source site coefficients could mitigate the bias caused by the lack of water and sedimentary layers in their seismic-wave numerical simulations. Our analytical Rayleigh-wave Green's function could also be applied to invert for the SM source distribution, similar to Xu et al. (2020), and to assess the uncertainty in this inversion (Xu & Mikesell, 2022).

6. Conclusion

We improve the modeling of secondary microseism (SM) PSDs by including lateral variations of ocean thickness and crustal structure. By incorporating source and receiver site 1D structures, including ocean, sediment, and crustal rocks, into our theoretical modeling, we are able to model important modulation effects of ocean-bottom sediments on exciting Rayleigh waves at the source sites and amplifying them at the receiver sites. Our WLHM modeling results agree well with field observations from ocean-bottom seismometers (OBSs) and permanent land stations, and this modeling is significantly more accurate than LH-SM modeling. Our methodology can provide predictions of SM energy levels at the global ocean bottom, thus aiding future seismic monitoring. It would benefit both seismic imaging of Earth's crust and research into the mechanical interactions between ocean gravity waves and shorelines.

Appendix A: Computation of Source and Receiver Site Coefficients Using Eigenfunction Theory

We assume a 1D structure—an ocean layer overlying a multiply layered crust—at a SM source and a receiver site. Rayleigh waves are assumed to propagate as plane waves in this structure as

$$\begin{bmatrix} r_1 \\ r_2 \\ r_3 \\ r_4 \end{bmatrix} \exp[i\omega(t - x/c)], \tag{A1}$$

where r_1 and r_2 represent the eigenfunctions of the horizontal- and vertical-component displacements, respectively; r_3 and r_4 are the eigenfunction of the shear and normal stresses, respectively (Aki & Richards, 2002). i is the imaginary unit. ω, t, x, and c are the angular frequency, the time, the horizontal distance, and Rayleigh-wave phase velocity, respectively. Full expressions of the horizontal and vertical displacements are written as $ir_1 \exp[i\omega(t - x/c)]$ and $r_2 \exp[i\omega(t - x/c)]$, respectively. Note that both the two displacement eigenfunctions and the corresponding phase and group velocities are required in computing source and receiver site coefficients (Equation 3).

We solve the Rayleigh-wave phase velocity by calculating the eigenfunctions for the ocean layer and the underlying crust separately. We set the origin at the ocean surface, defining the positive vertical direction as downward. We assume this ocean layer to be homogeneous, with density (ρ_w), acoustic-wave speed (α_w), water thickness (H), and zero shear modulus. Thus, in this layer, $r_3 = 0$, and we need only compute the other three eigenfunctions. For a trial phase velocity value (c_0) at a given frequency (f), this homogeneous-ocean-layer

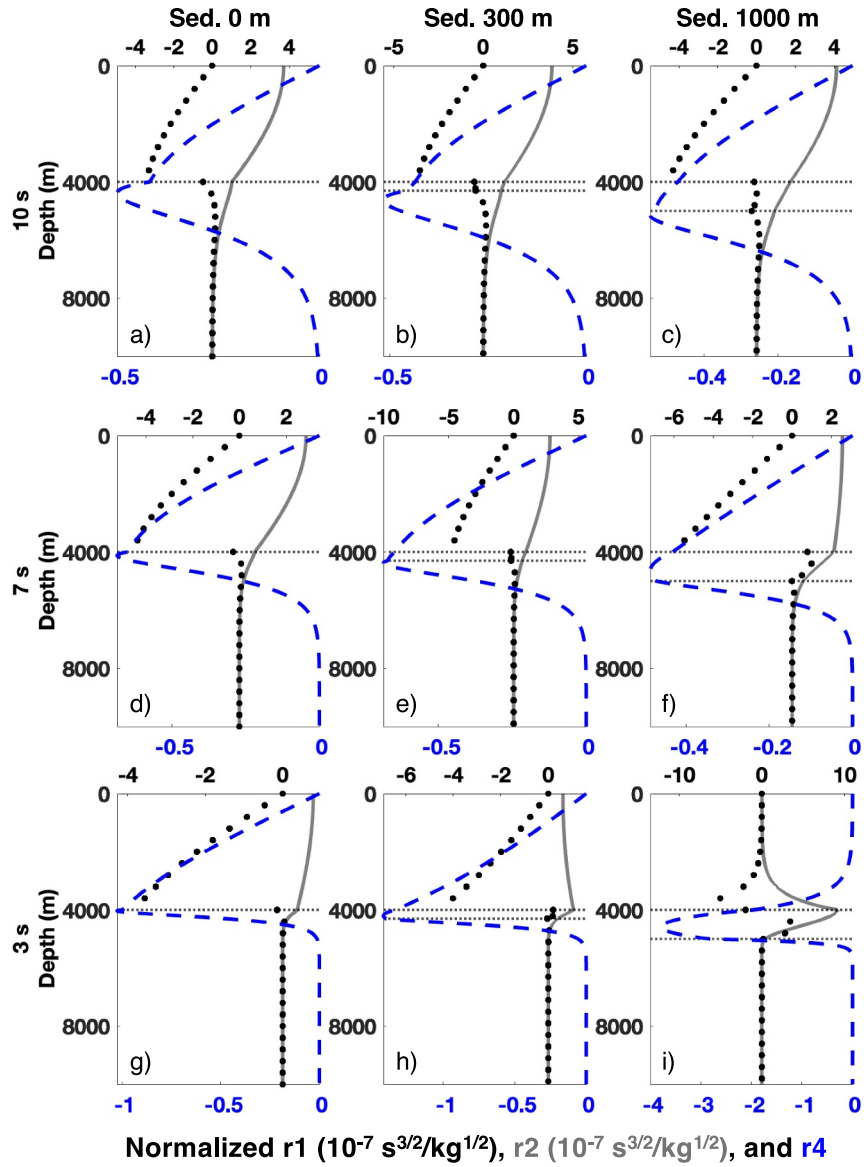

Figure A1. The Rayleigh-wave eigenfunctions for the velocity models with a 4,000-m-thick ocean layer as in Figure 1. The zero depth value represents the ocean surface. The eigenfunction values of each model at each frequency are normalized by the corresponding $\sqrt{4\pi f c U I_1}$. The unit of normalized r_4 is Pa $s^{3/2}$/(m $kg^{1/2}$). Dashed horizontal lines indicate the ocean bottom and the sediment layer bottom if this layer present. The eigenfunctions for a 1,000-m-thick ocean layer overlying the same crustal structure are displayed in Figure S3 in Supporting Information S1.

assumption indicates that only upgoing and downgoing acoustic waves can exist. This acoustic wavefield in a 2D Cartesian coordinate system is written as

$$p(\mathbf{x},\omega) = A_d \exp\left(i\omega t - ik_x x - ik_z z\right) + A_u \exp\left(i\omega t - ik_x x + ik_z z\right), \tag{A2}$$

$$= P(z)\exp(i\omega t - ik_x x), \tag{A3}$$

where p represents the pressure, and A_d and A_u are the amplitudes of the downgoing and upgoing waves, respectively. k_x accounts for the horizontal wavenumber and is equal to ω/c_0. We can write the variation of this pressure field in the vertical direction as

21699356, 2025, 5, Downloaded from https://agupubs.onlinelibrary.wiley.com/doi/10.1029/2024JB030767 by Portail BibCNRS INSU, Wiley Online Library on [11/06/2025]. See the Terms and Conditions (https://onlinelibrary.wiley.com/terms-and-conditions) on Wiley Online Library for rules of use; OA articles are governed by the applicable Creative Commons License

$$P(z) = A_d \exp(-ik_z z) + A_u \exp(ik_z z), \tag{A4}$$

where k_z is the vertical wavenumber and is defined as $\sqrt{(\omega/\alpha_w)^2 - k_x^2}$. Note that in our coordinate system, the ocean surface and bottom correspond to $z = 0$ and $z = H$, respectively. We rewrite ik_z as γ, where $\gamma = \omega\sqrt{1/c_0^2 - 1/\alpha_w^2}$ following Aki and Richards (2002, Chapter 7). To ensure that this wavefield satisfies the zero-pressure boundary condition at the ocean surface ($z = 0$), we choose a specific combination of A_d and A_u, such that:

$$P(z) = \exp(-\gamma z) - \exp(\gamma z). \tag{A5}$$

Note that $r_4 = -P$, because the positive directions of the acoustic pressure and normal stress are opposite at the ocean bottom boundary. According to Euler's equation:

$$-\begin{bmatrix}\partial_x \\ \partial_z\end{bmatrix} p = -\rho_w \omega^2 \begin{bmatrix} ir_1 \\ r_2 \end{bmatrix} \exp[i\omega(t - x/c)], \tag{A6}$$

where ∂_x and ∂_z denote the partial derivatives with respect to the directions of x and z, respectively, the two eigenfunctions are:

$$r_1 = -\frac{k_x P}{\rho_w \omega^2}, \tag{A7}$$

$$r_2 = \frac{\partial_z P}{\rho_w \omega^2}. \tag{A8}$$

This whole derivation is similar to the one in Xu et al. (2022).

We compute the eigenfunctions in the crust using the propagation matrix approach in Aki and Richards (2002, Chapter 7). These eigenfunctions need to satisfy two boundary conditions: zero shear stress at the top of the crust (i.e., the ocean bottom) and the radiation boundary condition at infinite depth. We adopt this approach and a trial phase velocity (c_0) as input to compute a wavefield satisfying these two boundary conditions (Xu & Lognonné, 2024). If c_0 is a correct phase velocity solution, the vertical compliance (r_2/r_4) at the ocean bottom should match $-r_2/P$ at the bottom of the ocean layer (Biot, 1952). Note that if an ocean-bottom sediment layer exists and its V_S value is lower than the acoustic-wave velocity of the ocean layer above, a guided Rayleigh wave would occur at a high frequency (i.e., 3 s period in Figure A1i), known as Scholte waves (Scholte, 1958).

The Rayleigh-wave phase velocity (c) at frequency f ensures the computation of r_1 and r_2 along the vertical direction. Subsequently, we compute the Rayleigh-wave energy (I_1) following:

$$I_1(f) = \frac{1}{2}\int_0^{+\infty} \rho(r_1^2 + r_2^2)\, dz, \tag{A9}$$

where this integral range is from the ocean surface (z_s) to infinite depth. We also compute the group velocity (U) as $d\omega/dk_x$, where $k_x = \omega/c$, using the phase velocities across a frequency band (Figure S2 in Supporting Information S1). Next, we calculate the source site coefficient as the ratio between r_2 at the ocean surface and $\sqrt{4\pi f c U I_1}$. The receiver site coefficient for OBS is the ratio between r_2 at the ocean bottom and $\sqrt{4\pi f c U I_1}$. For a land station, the receiver site coefficient is computed similarly to the above, and the corresponding computation of phase velocity and eigenfunction is identical to the classical Rayleigh-wave method (e.g., Aki & Richards, 2002).

21699356, 2025, 5, Downloaded from https://agupubs.onlinelibrary.wiley.com/doi/10.1029/2024JB030767 by Portail BibCNRS INSU, Wiley Online Library on [11/06/2025]. See the Terms and Conditions (https://onlinelibrary.wiley.com/terms-and-conditions) on Wiley Online Library for rules of use; OA articles are governed by the applicable Creative Commons License

Appendix B: Understanding Longuet-Higgins' Coefficients

Longuet-Higgins (1950) analytically computed the Green's function of a laterally homogeneous two-layer model, an ocean layer overlying a halfspace, and framed the amplitude as

$$W(X,\omega) = \frac{\sqrt{\omega}}{\rho_h \beta_h^{5/2} \sqrt{2\pi X}} \sqrt{\sum_i c_i^2}, \tag{B1}$$

where ρ_h and β_h denote the density and shear-wave velocity in this halfspace, respectively. X is the horizontal distance between the source and receiver in the 2D Cartesian coordinate system. c_i are unitless coefficients, corresponding to the i-th mode Rayleigh waves. The c_i values in Longuet-Higgins (1950) are computed from certain elastic model parameters (Table B1) and must be recalculated for different models.

The c_i coefficient has been interpreted as representing the SM source excitation (e.g., Ardhuin et al., 2015; Gualtieri et al., 2014; Igel et al., 2021; Stutzmann et al., 2012), but this interpretation does not reflect the entire physical meaning of the coefficient or the equation. For two-layer models (Table B1), the results of this equation align well with those of WLHM Green's function (Equation 3), as shown in Figure B1. This confirms that the c_i coefficient represents the product of the source and receiver site coefficients.

Table B1
The Two-Layer Model Parameters

Layer name	V_P (m/s)	V_S (m/s)	Density (kg/m^3)	Thickness (m)
Ocean	1,400	0	1,000	1,000/4,000
Halfspace	4,850	2,800	2,500	∞

Note. The acoustic/elastic parameters are from Longuet-Higgins (1950).

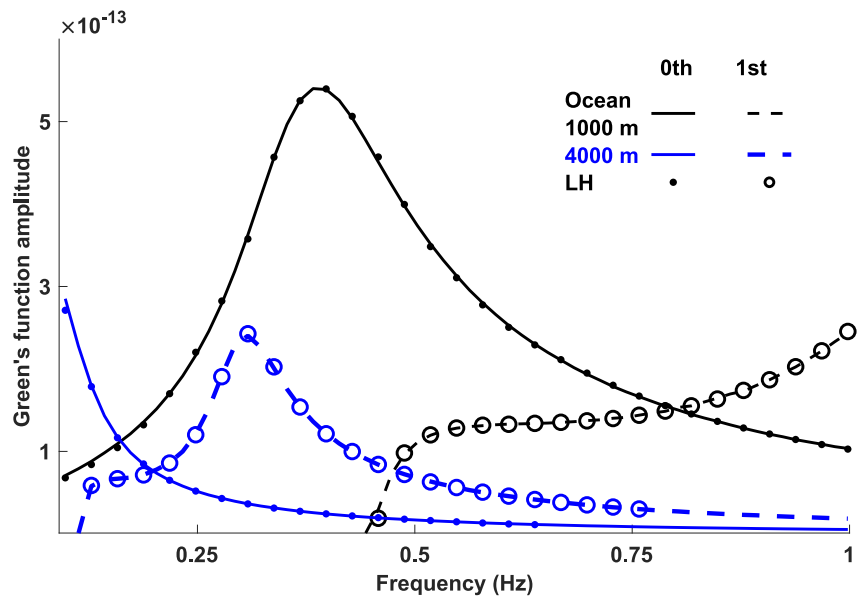

Figure B1. Computation results of Equation B1 (LH, Equation 186 in Longuet-Higgins (1950)) and Equation 3 for a two-layer model (curves). The ocean thickness is 1,000 or 4,000 m. This figure presents both the fundamental and 1st-higher mode Rayleigh-wave Green's function amplitude without the term: $\sqrt{X}$ (flat earth) or $\sqrt{R_E \sin(\Delta)}$ (spherical earth).

21699356, 2025, 5, Downloaded from https://agupubs.onlinelibrary.wiley.com/doi/10.1029/2024JB030767 by Portail BibCNRS INSU, Wiley Online Library on [11/06/2025]. See the Terms and Conditions (https://onlinelibrary.wiley.com/terms-and-conditions) on Wiley Online Library for rules of use; OA articles are governed by the applicable Creative Commons License

Data Availability Statement

We retrieve the CRUST1.0 model from https://doi.org/10.17611/DP/emccrust10. The computation code of source and receiver site coefficients is revised from Xu et al. (2022) and Xu and Lognonné (2024) and is available at Xu (2025). The SM pressure source PSD files are available at ftp://ftp.ifremer.fr/ifremer/ww3/HINDCAST/SISMO (Ardhuin et al., 2011). The seismic data used in this study are available through the IRIS Data Management Center (IRIS DMC) via Barruol et al. (2017) and Northern California Earthquake Data Center (2014), through European Plate Observing System France (EPOS-France) via Barruol et al. (2017) and Institut de physique du globe de Paris (IPGP) and Ecole et Observatoire des Sciences de la Terre de Strasbourg (EOST) (1982), through Ocean Hemisphere Project Data Management Center (OHPDMC) via Suetsugu et al. (2018).

Acknowledgments

The authors thank Prof. Robert Herrmann for his pointing to Rayleigh waves trapped in the ocean-bottom sediment layers in 1D models. The authors also thank Prof. Barbara Romanowicz for her introduction to the MOBB geological environment. The authors thank K.Yokoyama for his help in assessing PS OBS data. ZX thanks Jean Schmittbuhl, Martin Schimmel, Toshiro Tanimoto, and Dimitri Zigone for fruitful discussions. The authors thank editor Rachel Abercrombie, associate editor, and two anonymous reviewers for their constructive feedback. This research is funded by the ANR BRUIT-FM (ANR-21-CE01-0031).

References

Abercrombie, R. E. (1997). Near-surface attenuation and site effects from comparison of surface and deep borehole recordings. *Bulletin of the Seismological Society of America*, *87*(3), 731–744. https://doi.org/10.1785/bssa0870030731

Aki, K., & Richards, P. G. (2002). *Quantitative seismology*. Science Books.

Alday, M., & Ardhuin, F. (2023). On consistent parameterizations for both dominant wind-waves and spectral tail directionality. *Journal of Geophysical Research: Oceans*, *128*(4), e2022JC019581. https://doi.org/10.1029/2022jc019581

Ardhuin, F., Gualtieri, L., & Stutzmann, E. (2015). How ocean waves rock the Earth: Two mechanisms explain microseisms with periods 3 to 300 s. *Geophysical Research Letters*, *42*(3), 765–772. https://doi.org/10.1002/2014gl062782

Ardhuin, F., Gualtieri, L., Stutzmann, E., Nakata, N., & Fichtner, A. (2019). *Physics of ambient noise generation by ocean waves* (pp. 69–108). Seismic Ambient Noise.

Ardhuin, F., Lavanant, T., Obrebski, M., Marié, L., Royer, J.-Y., d'Eu, J.-F., et al. (2013). A numerical model for ocean ultra-low frequency noise: Wave-generated acoustic-gravity and Rayleigh modes. *Journal of the Acoustical Society of America*, *134*(4), 3242–3259. https://doi.org/10.1121/1.4818840

Ardhuin, F., & Roland, A. (2012). Coastal wave reflection, directional spread, and seismoacoustic noise sources. *Journal of Geophysical Research*, *117*(C11). https://doi.org/10.1029/2011jc007832

Ardhuin, F., Stutzmann, E., Schimmel, M., & Mangeney, A. (2011). Ocean wave sources of seismic noise. *Journal of Geophysical Research*, *116*(C09004), C09004. https://doi.org/10.1029/2011jc006952

Barruol, G., Sigloch, K., Group, R.-R., & RESIF. (2017). RHUM-RUM experiment, 2011-2015 [Dataset]. *RESIF*. https://doi.org/10.15778/RESIF.YV2011

Bensen, G. D., Ritzwoller, M. H., Barmin, M. P., Levshin, A. L., Lin, F., Moschetti, M. P., et al. (2007). Processing seismic ambient noise data to obtain reliable broad-band surface wave dispersion measurements. *Geophysical Journal International*, *169*(3), 1239–1260. https://doi.org/10.1111/j.1365-246x.2007.03374.x

Biot, M. A. (1952). The interaction of Rayleigh and Stoneley waves in the ocean bottom. *Bulletin of the Seismological Society of America*, *42*(1), 81–93. https://doi.org/10.1785/bssa0420010081

Booij, N., Holthuijsen, L., & Ris, R. (1996). The "SWAN" wave model for shallow water. *Coastal Engineering*, *1996*, 668–676. https://doi.org/10.1061/9780784402429.053

Boschi, L., Magrini, F., Cammarano, F., & van Der Meijde, M. (2019). On seismic ambient noise cross-correlation and surface-wave attenuation. *Geophysical Journal International*, *219*(3), 1568–1589. https://doi.org/10.1093/gji/ggz379

Bowden, D. C., & Tsai, V. C. (2017). Earthquake ground motion amplification for surface waves. *Geophysical Research Letters*, *44*(1), 121–127. https://doi.org/10.1002/2016gl071885

Bowden, D. C., Tsai, V. C., & Lin, F.-C. (2017). Amplification and attenuation across USArray using ambient noise wavefront tracking. *Journal of Geophysical Research: Solid Earth*, *122*(12), 10–086. https://doi.org/10.1002/2017jb014804

Cheng, F., Chi, B., Lindsey, N. J., Dawe, T. C., & Ajo-Franklin, J. B. (2021). Utilizing distributed acoustic sensing and ocean bottom fiber optic cables for submarine structural characterization. *Scientific Reports*, *11*(1), 5613. https://doi.org/10.1038/s41598-021-84845-y

Cotte, N., Pedersen, H., Campillo, M., Farra, V., & Cansi, Y. (2000). Off-great-circle propagation of intermediate-period surface waves observed on a dense array in the French Alps. *Geophysical Journal International*, *142*(3), 825–840. https://doi.org/10.1046/j.1365-246x.2000.00187.x

Crawford, W. C., Webb, S. C., & Hildebrand, J. A. (1991). Seafloor compliance observed by long-period pressure and displacement measurements. *Journal of Geophysical Research*, *96*(B10), 16151–16160. https://doi.org/10.1029/91jb01577

El Khoury, C. (2022). Seismic ambient noise amplitude anomalies induced by an anticline structure: Application to the context of gas reservoirs. *Theses, Université Paris sciences et lettres*. Retrieved from https://pastel.hal.science/tel-04510630

Erickson, D., McNamara, D. E., & Benz, H. M. (2004). Frequency-dependent Lg Q within the continental United States. *Bulletin of the Seismological Society of America*, *94*(5), 1630–1643. https://doi.org/10.1785/012003218

Ermert, L., Sager, K., Afanasiev, M., Boehm, C., & Fichtner, A. (2017). Ambient seismic source inversion in a heterogeneous Earth: Theory and application to the Earth's hum. *Journal of Geophysical Research: Solid Earth*, *122*(11), 9184–9207. https://doi.org/10.1002/2017jb014738

Ermert, L., Villasenor, A., & Fichtner, A. (2016). Cross-correlation imaging of ambient noise sources. *Geophysical Journal International*, *204*(1), 347–364. https://doi.org/10.1093/gji/ggv460

Farra, V., Stutzmann, E., Gualtieri, L., Schimmel, M., & Ardhuin, F. (2016). Ray-theoretical modeling of secondary microseism P waves. *Geophysical Journal International*, *206*(3), 1730–1739. https://doi.org/10.1093/gji/ggw242

Gerstoft, P., Shearer, P. M., Harmon, N., & Zhang, J. (2008). Global P, PP, and PKP wave microseisms observed from distant storms. *Geophysical Research Letters*, *35*(23). https://doi.org/10.1029/2008gl036111

Gimbert, F., & Tsai, V. C. (2015). Predicting short-period, wind-wave-generated seismic noise in coastal regions. *Earth and Planetary Science Letters*, *426*, 280–292. https://doi.org/10.1016/j.epsl.2015.06.017

Gualtieri, L., Stutzmann, É., Capdeville, Y., Farra, V., Mangeney, A., & Morelli, A. (2015). On the shaping factors of the secondary microseismic wavefield. *Journal of Geophysical Research: Solid Earth*, *120*(9), 6241–6262. https://doi.org/10.1002/2015jb012157

21699356, 2025, 5, Downloaded from https://agupubs.onlinelibrary.wiley.com/doi/10.1029/2024JB030767 by Portail BibCNRS INSU, Wiley Online Library on [11/06/2025]. See the Terms and Conditions (https://onlinelibrary.wiley.com/terms-and-conditions) on Wiley Online Library for rules of use; OA articles are governed by the applicable Creative Commons License

Gualtieri, L., Stutzmann, É., Farra, V., Capdeville, Y., Schimmel, M., Ardhuin, F., & Morelli, A. (2014). Modelling the ocean site effect on seismic noise body waves. *Geophysical Journal International*, *197*(2), 1096–1106. https://doi.org/10.1093/gji/ggu042

Hable, S., Sigloch, K., Stutzmann, E., Kiselev, S., & Barruol, G. (2019). Tomography of crust and lithosphere in the western Indian Ocean from noise cross-correlations of land and ocean bottom seismometers. *Geophysical Journal International*, *219*(2), 924–944. https://doi.org/10.1093/gji/ggz333

Hasselmann, K. (1963). A statistical analysis of the generation of microseisms. *Reviews of Geophysics*, *1*(2), 177–210. https://doi.org/10.1029/rg001i002p00177

Ide, S., Beroza, G. C., Shelly, D. R., & Uchide, T. (2007). A scaling law for slow earthquakes. *Nature*, *447*(7140), 76–79. https://doi.org/10.1038/nature05780

Igel, J. K., Bowden, D. C., & Fichtner, A. (2023). SANS: Publicly available daily multi-scale seismic ambient noise source maps. *Journal of Geophysical Research: Solid Earth*, *128*(1), e2022JB025114. https://doi.org/10.1029/2022jb025114

Igel, J. K., Ermert, L. A., & Fichtner, A. (2021). Rapid finite-frequency microseismic noise source inversion at regional to global scales. *Geophysical Journal International*, *227*(1), 169–183. https://doi.org/10.1093/gji/ggab210

Institut de physique du globe de Paris (IPGP) and Ecole et Observatoire des Sciences de la Terre de Strasbourg (EOST). (1982). *GEOSCOPE, French Global Network of broad band seismic stations*. Institut de physique du globe de Paris (IPGP), Université de Paris. https://doi.org/10.18715/GEOSCOPE.G

Kaneko, L., Ide, S., & Nakano, M. (2018). Slow earthquakes in the microseism frequency band (0.1–1.0 Hz) off Kii Peninsula, Japan. *Geophysical Research Letters*, *45*(6), 2618–2624. https://doi.org/10.1002/2017gl076773

Kedar, S., Longuet-Higgins, M., Webb, F., Graham, N., Clayton, R., & Jones, C. (2008). The origin of deep ocean microseisms in the North Atlantic Ocean. *Proceedings of the Royal Society A: Mathematical, Physical and Engineering Sciences*, *464*(2091), 777–793. https://doi.org/10.1098/rspa.2007.0277

Keilis-Borok, V. (1989). Surface waves in media with weak lateral inhomogeneity. In *Seismic surface waves in a laterally inhomogeneous Earth* (pp. 35–69). Springer.

Kubo, H., Nakamura, T., Suzuki, W., Kimura, T., Kunugi, T., Takahashi, N., & Aoi, S. (2018). Site amplification characteristics at Nankai seafloor observation network, DONET1, Japan, evaluated using spectral inversion. *Bulletin of the Seismological Society of America*, *108*(3A), 1210–1218. https://doi.org/10.1785/0120170254

Laske, G., Masters, G., Ma, Z., & Pasyanos, M. (2012). CRUST1. 0: An updated global model of Earth's crust. *Geophys res abs*, *14*(3), 743.

Le Pape, F., Craig, D., & Bean, C. J. (2021). How deep ocean-land coupling controls the generation of secondary microseism Love waves. *Nature Communications*, *12*(1), 2332. https://doi.org/10.1038/s41467-021-22591-5

Lin, F.-C., Moschetti, M. P., & Ritzwoller, M. H. (2008). Surface wave tomography of the western United States from ambient seismic noise: Rayleigh and Love wave phase velocity maps. *Geophysical Journal International*, *173*(1), 281–298. https://doi.org/10.1111/j.1365-246x.2008.03720.x

Lindsey, N. J., Dawe, T. C., & Ajo-Franklin, J. B. (2019). Illuminating seafloor faults and ocean dynamics with dark fiber distributed acoustic sensing. *Science*, *366*(6469), 1103–1107. https://doi.org/10.1126/science.aay5881

Longuet-Higgins, M. S. (1950). A theory of the origin of microseisms. *Philosophical Transactions of the Royal Society of London - Series A: Mathematical and Physical Sciences*, *243*(857), 1–35.

Lynner, C., Van Avendonk, H. J., Bécel, A., Christeson, G. L., Dugan, B., Gaherty, J. B., et al. (2020). The eastern North American margin community seismic experiment: An amphibious active-and passive-source dataset. *Seismological Research Letters*, *91*(1), 533–540. https://doi.org/10.1785/0220190142

Meschede, M., Stutzmann, É., Farra, V., Schimmel, M., & Ardhuin, F. (2017). The effect of water column resonance on the spectra of secondary microseism P waves. *Journal of Geophysical Research: Solid Earth*, *122*(10), 8121–8142. https://doi.org/10.1002/2017jb014014

Nakamura, T., Nakano, M., Hayashimoto, N., Takahashi, N., Takenaka, H., Okamoto, T., et al. (2014). Anomalously large seismic amplifications in the seafloor area off the Kii peninsula. *Marine Geophysical Researches*, *35*(3), 255–270. https://doi.org/10.1007/s11001-014-9211-2

Nishida, K., & Takagi, R. (2016). Teleseismic S wave microseisms. *Science*, *353*(6302), 919–921. https://doi.org/10.1126/science.aaf7573

Noguchi, S., Maeda, T., & Furumura, T. (2016). Ocean-influenced Rayleigh waves from outer-rise earthquakes and their effects on durations of long-period ground motion. *Geophysical Journal International*, *205*(2), 1099–1107. https://doi.org/10.1093/gji/ggw074

Northern California Earthquake Data Center. (2014). *Berkeley digital seismic network (BDSN)*. Author. https://doi.org/10.7932/NCEDC

Pavlis, G. L., & Mahdi, H. (1996). Surface wave propagation in central Asia: Observations of scattering and multipathing with the Kyrgyzstan broadband array. *Journal of Geophysical Research*, *101*(B4), 8437–8455. https://doi.org/10.1029/95jb03449

Peterson, J. R. (1993). *Observations and modeling of seismic background noise* (Tech. Rep.). US Geological Survey. https://doi.org/10.3133/ofr93322

Prieto, G., Lawrence, J., & Beroza, G. (2009). Anelastic Earth structure from the coherency of the ambient seismic field. *Journal of Geophysical Research*, *114*(B7). https://doi.org/10.1029/2008jb006067

Romanowicz, B., Allen, R., Brekke, K., Chen, L.-W., Gou, Y., Henson, I., et al. (2023). SeaFOAM: A year-long DAS deployment in Monterey Bay, California. *Seismological Research Letters*, *94*(5), 2348–2359. https://doi.org/10.1785/0220230047

Romanowicz, B., Stakes, D., Dolenc, D., Neuhauser, D., McGill, P., Uhrhammer, R., et al. (2006). The Monterey Bay broadband ocean bottom seismic observatory. *Annals of Geophisycs*.

Romero, L. (2019). Distribution of surface wave breaking fronts. *Geophysical Research Letters*, *46*(17–18), 10463–10474. https://doi.org/10.1029/2019gl083408

Ruan, Y., Forsyth, D. W., & Bell, S. W. (2014). Marine sediment shear velocity structure from the ratio of displacement to pressure of Rayleigh waves at seafloor. *Journal of Geophysical Research: Solid Earth*, *119*(8), 6357–6371. https://doi.org/10.1002/2014jb011162

Scholte, J. G. J. (1958). Rayleigh waves in isotropic and anistropic elastic media. *Meded. Verhand. KNMI*, *72*, 9–43.

Shapiro, N. M., Campillo, M., Stehly, L., & Ritzwoller, M. H. (2005). High-resolution surface-wave tomography from ambient seismic noise. *Science*, *307*(5715), 1615–1618. https://doi.org/10.1126/science.1108339

Shen, W., Ritzwoller, M. H., Kang, D., Kim, Y., Lin, F.-C., Ning, J., et al. (2016). A seismic reference model for the crust and uppermost mantle beneath China from surface wave dispersion. *Geophysical Journal International*, *206*(2), 954–979. https://doi.org/10.1093/gji/ggw175

Snieder, R., & Nolet, G. (1987). Linearized scattering of surface waves on a spherical Earth. *Journal of Geophysics*, *61*(1), 55–63.

Stähler, S. C., Sigloch, K., Hosseini, K., Crawford, W. C., Barruol, G., Schmidt-Aursch, M. C., et al. (2016). Performance report of the RHUM-RUM ocean bottom seismometer network around La Réunion, western Indian Ocean. *Advances in Geosciences*, *41*, 43–63. https://doi.org/10.5194/adgeo-41-43-2016

Stutzmann, E., Ardhuin, F., Schimmel, M., Mangeney, A., & Patau, G. (2012). Modelling long-term seismic noise in various environments. *Geophysical Journal International*, *191*(2), 707–722. https://doi.org/10.1111/j.1365-246x.2012.05638.x

21699356, 2025, 5, Downloaded from https://agupubs.onlinelibrary.wiley.com/doi/10.1029/2024JB030767 by Portail BibCNRS INSU, Wiley Online Library on [11/06/2025]. See the Terms and Conditions (https://onlinelibrary.wiley.com/terms-and-conditions) on Wiley Online Library for rules of use; OA articles are governed by the applicable Creative Commons License

Suetsugu, D., Shiobara, H., Sugioka, H., Tada, N., Ito, A., Isse, T., et al. (2018). The OJP array: Seismological and electromagnetic observation on seafloor and islands in the Ontong Java Plateau. *JAMSTEC Report of Research and Development*, *26*(0), 54–64. https://doi.org/10.5918/jamstecr.26.54

Takemura, S., Emoto, K., & Yamaya, L. (2023). High-frequency S and S-coda waves at ocean-bottom seismometers. *Earth Planets and Space*, *75*(1), 20. https://doi.org/10.1186/s40623-023-01778-8

Tromp, J., & Dahlen, F. (1992). Variational principles for surface wave propagation on a laterally heterogeneous Earth—II. Frequency-domain jwkb theory. *Geophysical Journal International*, *109*(3), 599–619. https://doi.org/10.1111/j.1365-246x.1992.tb00120.x

Tsai, V. C. (2011). Understanding the amplitudes of noise correlation measurements. *Journal of Geophysical Research*, *116*(B9), B09311. https://doi.org/10.1029/2011jb008483

Viegas, G. M., Baise, L. G., & Abercrombie, R. E. (2010). Regional wave propagation in New England and New York. *Bulletin of the Seismological Society of America*, *100*(5A), 2196–2218. https://doi.org/10.1785/0120090223

Viens, L., Denolle, M., Miyake, H., Sakai, S., & Nakagawa, S. (2017). Retrieving impulse response function amplitudes from the ambient seismic field. *Geophysical Journal International*, *210*(1), 210–222. https://doi.org/10.1093/gji/ggx155

Wavewatch III Development Group. (2016). *User manual and system documentation of wavewatch III version 5.16* (Vol. 329, pp. 1–326). NOAA/NWS/NCEP/MMAB Technical Note.

Webb, S. C. (1998). Broadband seismology and noise under the ocean. *Reviews of Geophysics*, *36*(1), 105–142. https://doi.org/10.1029/97rg02287

Webb, S. C., & Crawford, W. C. (2010). Shallow-water broadband OBS seismology. *Bulletin of the Seismological Society of America*, *100*(4), 1770–1778. https://doi.org/10.1785/0120090203

Woodhouse, J. (1974). Surface waves in a laterally varying layered structure. *Geophysical Journal International*, *37*(3), 461–490. https://doi.org/10.1111/j.1365-246x.1974.tb04098.x

Woodhouse, J., & Wong, Y. (1986). Amplitude, phase and path anomalies of mantle waves. *Geophysical Journal International*, *87*(3), 753–773. https://doi.org/10.1111/j.1365-246x.1986.tb01970.x

Xia, Y., Ni, S., & Tape, C. (2018). Multipathing Rayleigh waves from long-distance noise cross correlation along an ocean-continent boundary (Alaska to California). *Geophysical Research Letters*, *45*(12), 6051–6060. https://doi.org/10.1029/2018gl077169

Xu, Z. (2025). MATLAB codes for "Theoretical Modelling of Secondary Microseisms Considering Source and Receiver Site Structures, with a Focus on Ocean-Bottom Sediment Effects" [Software]. *Zenodo*. https://doi.org/10.5281/zenodo.14832782

Xu, Z., Froment, M., Garcia, R. F., Beucler, É., Onodera, K., Kawamura, T., et al. (2022). Modeling seismic recordings of high-frequency guided infrasound on Mars. *Journal of Geophysical Research: Planets*, *127*(11), e2022JE007483. https://doi.org/10.1029/2022je007483

Xu, Z., & Lognonné, P. (2024). A comprehensive theory for 1-D (an) elastic medium deformation due to plane-wave fluid pressure perturbation. *Geophysical Journal International*, *236*(3), 1499–1512. https://doi.org/10.1093/gji/ggae005

Xu, Z., & Mikesell, T. D. (2022). Estimation of resolution and covariance of ambient seismic source distributions: Full waveform inversion and matched field processing. *Journal of Geophysical Research: Solid Earth*, *127*(6), e2022JB024374. https://doi.org/10.1029/2022jb024374

Xu, Z., Mikesell, T. D., Umlauft, J., & Gribler, G. (2020). Rayleigh-Wave multicomponent crosscorrelation-based source strength distribution inversions. Part 2: A workflow for field seismic data. *Geophysical Journal International*, *222*(3), 2084–2101. https://doi.org/10.1093/gji/ggaa284

Yarce, J., Sheehan, A., Nakai, J., Schwartz, S., Mochizuki, K., Savage, M., et al. (2019). Seismicity at the northern Hikurangi Margin, New Zealand, and investigation of the potential spatial and temporal relationships with a shallow slow slip event. *Journal of Geophysical Research: Solid Earth*, *124*(5), 4751–4766. https://doi.org/10.1029/2018jb017211

Ying, Y., Bean, C. J., & Bromirski, P. D. (2014). Propagation of microseisms from the deep ocean to land. *Geophysical Research Letters*, *41*(18), 6374–6379. https://doi.org/10.1002/2014gl060979

Zha, Y., & Webb, S. C. (2016). Crustal shear velocity structure in the Southern Lau Basin constrained by seafloor compliance. *Journal of Geophysical Research: Solid Earth*, *121*(5), 3220–3237. https://doi.org/10.1002/2015jb012688

Zhou, Y., Dahlen, F., & Nolet, G. (2004). Three-dimensional sensitivity kernels for surface wave observables. *Geophysical Journal International*, *158*(1), 142–168. https://doi.org/10.1111/j.1365-246x.2004.02324.x

21699356, 2025, 5, Downloaded from https://agupubs.onlinelibrary.wiley.com/doi/10.1029/2024JB030767 by Portail BibCNRS INSU, Wiley Online Library on [11/06/2025]. See the Terms and Conditions (https://onlinelibrary.wiley.com/terms-and-conditions) on Wiley Online Library for rules of use; OA articles are governed by the applicable Creative Commons License